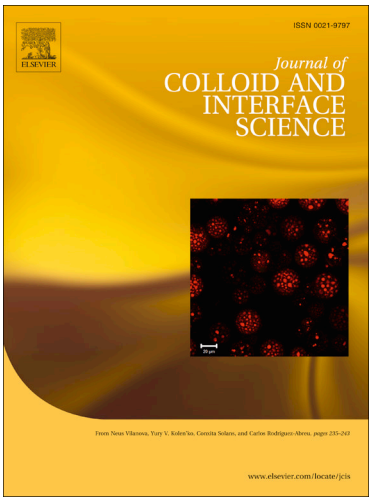

Regular Article

Peroxidase mimetic activity of Fe_3O_4 nanoparticle prepared based on magnetic hydrogels for hydrogen peroxide and glucose detection

Shasha Song, Yang Liu, Aixin Song, Zengdian Zhao, Hongsheng Lu, Jingcheng Hao

PII: S0021-9797(17)30795-6
DOI: http://dx.doi.org/10.1016/j.jcis.2017.07.029
Reference: YJCIS 22558

To appear in: *Journal of Colloid and Interface Science*

Received Date: 27 March 2017
Revised Date: 5 July 2017
Accepted Date: 8 July 2017

Please cite this article as: S. Song, Y. Liu, A. Song, Z. Zhao, H. Lu, J. Hao, Peroxidase mimetic activity of Fe_3O_4 nanoparticle prepared based on magnetic hydrogels for hydrogen peroxide and glucose detection, *Journal of Colloid and Interface Science* (2017), doi: http://dx.doi.org/10.1016/j.jcis.2017.07.029

Peroxidase mimetic activity of Fe_3O_4 nanoparticle prepared based on magnetic hydrogels for hydrogen peroxide and glucose detection

Shasha Song,*[a] Yang Liu,[a] Aixin Song,[b] Zengdian Zhao,[a] Hongsheng Lu[c] and Jingcheng Hao[b]

[a]School of Chemical Engineering, Shandong University of Technology, Zibo, 255000, P. R. China

[b]Key Laboratory of Colloid and Interface Chemistry & Key Laboratory of Special Aggregated Materials, Shandong University, Ministry of Education, Jinan, 250100, P. R. China

[c]Oil & Gas Field Applied Chemistry Key Laboratory of Sichuan Province, Southwest Petroleum University, Chengdu, 610500, P. R. China

* To whom correspondence should be addressed.

S.S., e-mail: songshasha@sdut.edu.cn.

ABSTRACT: Stimuli-response magnetic hydrogels were prepared in the mixtures of magnetic surfactants, (C_nTAFB(C), n = 12, 14, 16), and chiral amphiphiles, sodium cholate (SC). The gelation behavior of C_nTAFB(C)/SC were studied in detail. The results proved that the hydrophobicity of surfactants and the hydration radius (R_h) of anions played a vital role in the gelation process. The microstructure of the hydrogels were determined to be three-dimensional network of fibrous aggregates. The formation of the hydrogel fibrils was considered to be mainly driven by a delicate balance of multiple non-convalent interactions including hydrophobic interaction, electrostatic interaction, hydrogen bonding, van der Waals force, and the steric effect of SC molecule. Rheological measurements demonstrated that the hydrogels are high mechanical strength materials (the yield stress exceeding 2000 Pa). The mechanical strength of the hydrogels is dependent on the fiber density, which can be regulated by changing the proportion of the two compounds, the total concentration and the chain length of the surfactants. The magnetic hydrogels of C_{12}TAFB/SC mixtures served as the precursors for preparing cubic Fe_3O_4 nanoparticles with the diameter of 7.2 nm. The as-prepared Fe_3O_4 nanoparticles exhibit excellent ferromagnetic characteristic and high peroxidase-like activity and can be used as biosensor for hydrogen peroxide (H_2O_2) and glucose detection. We developed a convenient and green method for preparing Fe_3O_4 nanoparticles, which can be used as a promising candidate biosensor for glucose detection.

KEYWORDS: *hydrogels, biosensor, peroxidase mimetic activity, Fe_3O_4 nanoparticles, glucose detection*

1. Introduction

Gels are commonplace household materials, which have permeated our daily life in various kinds of forms such as hair gel, shampoo, toothpaste, and other cosmetic [1]. Among various gels, hydrogels formed by functional surfactant molecules aroused tremendous interest, owing to their potential applications in the fields of biology, material, environment and biomedicine science. The main driving forces for thr formation of surfactant hydrogels are noncovalent interactions (including hydrogen bonding, hydrophobic interaction, electrostatic interaction, π-π interaction, etc.) [2-8]. The weak and reversible nature of the non-covalent interactions endow the surfactant hydrogels respond to external stimulus, such as temperature, pH, light, and redox reactions [2,9]. Moreover, surfactant hydrogels are green soft materials, composed of large amounts of water (> 95 wt%) and small part of organic species, which can be used to imitate the physical properties of soft tissues (such as cartilage, muscle, and eyeball), and can be applied to diapers, contact lenses, and drug reservoirs [10]. Nowadays, one of the challenge for surfactant hydrogels is the design of novel surfactants with special functional groups for constructing hydrogels with fascinating structures to achieve functional applications [11].

The biocompatibility of hydrogels is crucial for biologically directed applications and environmental considerations [1]. Bile salts, the end product of the metabolism of cholesterol with several chiral centers and a rigid hydrophobic steroid nucleus, are produced by liver and stored in gallbladder [12-14]. The particular role and specific molecular structure render bile salts and its derivatives novel and abundant self-assembly behavior, which has been gradually investigated in recent decades [1,15]. The tubular structures as a thermal stable state were found in alkaline solutions of sodium or ammonium salts of lithocholic acid (LCA) [13,14,16-18]. In addition,

hydrogels were observed by mixing LCA with metal ions or organic amines [4,8,19,20].

Peroxidase activity is very important for many biochemical assays, due to their wide application in biomedical and environmental monitoring [21]. Currently, most of the peroxidase enzyme used for assays is horse radish peroxidase (HRP). Although HRP have high catalysis efficiency under very mild and friendly conditions, its applications is restricted due to its intrinsic properties such as sensitivity of catalytic activity to environmental condition and relativity low stability (denaturation and digestion) [22-24]. Therefore, tremendous efforts have been expended to construct enzyme mimetics [25,26,27]. Over the past few decades, a series of nanomaterials, such as graphene oxide (GO) [28], carbon nanotubes [29], carbon dots [30], bimetallic alloy nanostructures [31], nanoceria [32], FeS [33], and gold nanoparticles [34], have been found to exhibit unexpected peroxidase enzyme-like activity [35]. Among the nanomaterials, Fe_3O_4 magnetic nanoparticles (MNPs) have been considered as the most important peroxidase-like nanozyme and received the most attention, due to their high chemical stability, feasible surface modification, and excellent chemically and biologically inert [36,37]. However, the preparation of morphology controllable Fe_3O_4 MNPs is still a challenge. Current methods for fabricating morphology controllable Fe_3O_4 MNPs, including a hydrothermal process, solvothermal process and thermal decomposition [38,39], involve toxic sources (organic solvents) and rigorous conditions (e.g., a high reaction temperature, high pressure), preventing the large-scale production and widespread practical applications. Therefore, nontoxic, water-based approaches are urgently needed to prepare morphology controllable Fe_3O_4 MNPs.

Herein, we developed a convenient, water-based approach for the preparation of

Fe_3O_4 MNPs based on magnetic hydrogels to study their peroxidase mimetic activity and explore their applications in biocatalysis and biosensing. The magnetic hydrogels were obtained by mixing C_nTAFB and SC in water. The gelation behavior of C_nTAFB(C)/SC system demonstrated that the hydrophobicity of surfactant and hydration radius (R_h) of anions play crucial role in the gelation. The hydrogels were formed by fibrils with the uniform diameter of 30 nm. Rheological results demonstrated that the hydrogels are high mechanical strength materials, which can be regulated by changing the proportion of the two compounds, the total concentration and the hydrophobic chain length of surfactants. The hydrogels can serve as the precursors to prepare cubic Fe_3O_4 MNPs with the diameter of 7.2 nm. The as-prepared Fe_3O_4 MNPs exhibited excellent ferromagnetic property and higher catalytic activity, which can be used as biosensor for H_2O_2 and glucose detection.

2. Experimental section

2.1. Chemicals and materials

The cationic surfactant, $CH_3(CH_2)_{n-2}CH_2N(CH_3)_3[FeCl_4]$ (C_nTAFC, n = 12, 14, and 16) and $CH_3(CH_2)_{n-2}CH_2N(CH_3)_3[FeBrCl_3]$ (C_nTAFB, n = 12, 14, and 16), were synthesized according to the literature [40-42] by mixing equal molar amount of cationic surfactant, $CH_3(CH_2)_{n-2}CH_2N(CH_3)_3Cl$ (C_nTAC, n = 12, 14, and 16) and $CH_3(CH_2)_{n-2}CH_2N(CH_3)_3Br$ (C_nTAB, n = 12, 14, and 16), with iron trichloride ($FeCl_3$) in methanol and stirring overnight at room temperature. The solvent was then removed and the product dried at reduced pressure at 80 ^oC overnight yield brown/red solid. After the reaction, the Cl^- or Br^- can be converted to $[FeCl_4]^-$ or $[FeCl_3Br]^-$. C_nTAB (n= 12, 14, 16), $FeCl_3$, sodium hydroxide (NaOH), hydrogen peroxide (H_2O_2, 30 wt %), sodium acetate, and acetic acid were purchased from Sinopharm Chemical

Reagent Co. Ltd. (Shanghai, China). C_nTAC (n= 12, 14, 16), sodium cholate (SC, >98%), sodium deoxycholate (SDC, >98%), and glucose oxidase (GOx) were purchased from J&K Chemical Company, Ltd. (Beijing, China). Horseradish peroxidase (HRP) was purchased from Sigma–Aldrich. All the chemicals were used without further purification. Ultrapure water with a resistivity of 18.25 mΩ·cm was obtained using a UPH-IV ultrapure water purifier (Chengdu Ultrapure Technology Co. Ltd., China).

2.2. Gelation behavior study

The samples were prepared by mixing appropriate amounts of SC (SDC or SLC) and C_nTAFC (n = 12, 14, 16) or C_nTAFB (n = 12, 14, 16) in water, and followed by stirring at 40 ^oC. Then, the samples were equilibrated at T = 25.0 ± 0.1 ^oC for at least 4 weeks before the gelation behavior was inspected.

2.3. Methods and characterizations

For transmission electron microscopy (TEM) observation, small volume of gel sample was placed on TEM grids (copper grid, 3.02 mm, 200 meshes, coated with formvar film) and the excess sample was wiped away with a filter paper. The copper grids were frozen in a vacuum extractor at -55 °C for several days. Then the copper grids were observed on a JEOL JEM-1400 TEM operating at 120 kV. The images were recorded on a Gatan multiscan CCD and processed with digital micrograph. Fe_3O_4 MNPs were observed through a JEOL JEM-2010 high-resolution TEM (Japan) at an acceleration voltage of 200 kV.

Rheological measurements were performed on a HAAKE RS6000 rheometer with a cone-plate system (C35/1° Ti L07116 at 25.0 ± 0.1 °C, diameter: 35 mm, cone angle: 1°). The viscoelastic properties of the hydrogels were determined by using oscillatory

measurements with an amplitude sweep in the frequency range of 0.01 to 10 Hz. Prior to the frequency sweep, the linear viscoelastic region was determined by stress-sweep measurements.

Phase transition temperature was obtained from DSC8500 (PerkinElmer, USA). The heating rate was set as 2.5 °C·min^{-1}.

The XRD patterns were recorded using a Rigaku D/Max 2200-PC diffractometer with Cu Kα radiation (λ= 0.15418 nm) and a graphite monochromator. The samples were measured at room temperature in the 2θ scan mode (2.5° min^{-1}).

The FT-IR spectra over the range of 4000 – 400 cm^{-1} were obtained on a VERTEX-70/70v FT-IR spectrometer (Bruker Optics, Germany) by taking 64 scans with a final resolution of 4 cm^{-1}. Spectral manipulation was performed by using the OPUS 6.5 software package (Bruker Optics, Germany). The sample was mixed with KBr and pressed into a plate for the measurements.

2.4. Fe_3O_4 magnetic nanoparticles (MNPs) preparation

As-prepared hydrogel was immersed in an aqueous solution of iron ions with a molar ratio of [Fe^{2+}]/[Fe^{3+}] = 11:1 for 12 h. The hydrogels loaded with iron ions were subsequently transferred into sodium hydroxide (NaOH) aqueous solution (0.5 mol·L^{-1}) and kept at 50 ^{o}C in water bath for 12 h, resulting in the precipitation of Fe_3O_4 MNPs.

2.5. Mimetic peroxidase activity assays

HRP-like activity was examined using TMB as a chromogenic substrate. Catalytic assays experiments were carried out using 50 μg Fe_3O_4 MNPs or 1 ng HRP in acetate buffer (8 mL, 0.2 mol·L^{-1}, pH = 4.0) in the presence of 530 mmol·L^{-1} H_2O_2 for Fe_3O_4 MNPs and 8.8 mmol·L^{-1} for HRP, using 816 μmol·L^{-1} TMB as the substrate at 40 ^{o}C

for 1 h [27]. After the reactions, the color formation was monitored at 652 nm using a HITACHIU-4100 spectrophotometer with the scan rate of 600 nm·min^{-1}.

The reaction kinetics for the catalytic oxidation of TMB was carried out by recording the absorption spectra at 652 nm. The apparent kinetic parameters were calculated based on the Michaelis equation: $v = V_{max} \times [S]/(K_m + [S])$ (1),

where v is the initial velocity, V_{max} is the maximal reaction velocity, [S] is the concentration of substrate and K_m is the Michaelis constant. K_m and V_{max} were obtained by the Lineweavere-Burk plot method. To investigate the mechanism, assays were carried out under standard reaction conditions as described above by varying concentrations of TMB at a fixed concentration of H_2O_2 or vice versa.

2.6. H_2O_2 and glucose detection

H_2O_2 detection was performed using the Fe_3O_4 MNPs in substrate solution with various H_2O_2 concentrations (0.01 μmol·L^{-1} – 1 mol·L^{-1}). After the reactions, the substrate solutions were monitored at 652 nm using HITACHIU-4100 spectrophotometer with the scan rate of 600 nm·min^{-1}.

Glucose detection was performed as follows: (i) 0.1 mL GOx (1 mg·mL^{-1}) and 0.1 mL different concentrations of glucose in 10 mmol·L^{-1} acetate buffer (pH = 7.0) were incubated at 37 ^{o}C for 30 min; (ii) 0.25 mL TMB (1 mmol·L^{-1}), 0.1 mL Fe_3O_4 MNPs (175 mg·L^{-1}), and 3.95 mL acetate buffer (0.2 mol·L^{-1}, pH = 4.0) were added into the glucose reaction solution; (iii) the mixture solution was incubated in 40 ^{o}C water bath for 20 min, and the final reaction solution was used to perform the adsorption spectroscopy measurement at 652 nm. In control experiments, 10 mmol·L^{-1} maltose, 10 mmol·L^{-1} lactose, and 10 mmol·L^{-1} fructose were used instead of glucose, under conditions identical to those reported above.

3. Results and discussion

3.1. Gelation behavior

Magnetic hydrogels (the magnetic property of hydrogels was shown in Figure S1) was obtained by heating the mixtures of magnetic surfactant, C_nTAFB(C) (n = 12, 14, 16), and SC to 40 ^oC and cooling the mixtures to room temperature (R.T). In order to explore the influence of hydrophobicity of surfactant and hydration radius (R_h) of anions on the gelation, the gelation behavior of SC/C_nTAFB(C) system was investigated in detail. The remarkable differences in gelation behaviors of the mixtures were listed in Table 1. From Table 1, one can see that the *CGC* and gelation time decrease with the increase in hydrophobic chain length of C_nTAFB(C), which is attributed to the increment of hydrophobic interaction facilitate the assembly of gelators to form gel [43,44]. The hydrophobic interaction in the mixtures can also be regulated by changing the number of hydroxyl in steroid nucleus of sodium salts of bile acid. As the number of hydroxyl group reduces, the hydrophobicity of gelator increases, causing the decrease of *CGC*. The gelation process is a balance between crystallization and solubilization, and the hydrogel is the results of a delicate balance between hydrophobicity and hydrophilicity [45,46]. Thus, SLC can not form hydrogel with C_nTAFB(C) due to the too high hydrophobicity, and only precipitates obtained. The hydration of anions also has a pronounced effect on the gelator assembly [47,48]. Cl^- is well hydrated anion, ascribed to kosmotrope, and Br^- is poorly hydrated anions, being referred as chaotropes [49]. Thus, C_nTAFB was easier to aggregate to form gels with SC than C_nTAFC, presenting lower *CGC* and higher gelation ability. In the present work, we mainly focused on C_nTAFB/SC system, and studied their gelation

properties and self-assembly process.

Table 1 Gelation behavior of C_nTAFB(C) and sodium salts of bile acid systems in aqueous solutions at 25 ^oC

	Chain length (nm) [50]	**Aggregates**			***CGC*[a] (wt %)**			**Gelation time**			**Gelation number[b]**		
		SC	SDC	SLC	SC	SDC	SLC	SC	SDC	SLC	SC	SDC	SLC
C_{12}TAFB	1.672	G[c]	G	P[d]	0.329	0.282		48 h	96 h		7936	9259	
C_{12}TAFC	1.672	G	G	P	0.320	0.270		72 h	108 h		7407	8547	
C_{14}TAFB	1.925	G	G	P	0.249	0.224		36 h	48 h		11111	12345	
C_{14}TAFC	1.925	G	G	P	0.250	0.227		40 h	54 h		10101	11111	
C_{16}TAFB	2.178	G	G	P	0.211	0.184		30 h	36 h		13888	14873	
C_{16}TAFC	2.178	G	G	P	0.217	0.193		36 h	48 h		12345	13888	

[a]*CGC*: critical gelation concentration; [b]Gelation number: the maximum number of solvent molecules immobilized by gelator molecules [44]; [c]G: Gels; [d]P: precipitates.

Fig. 1 shows the phase diagram of C_nTAFB/SC system, which is certified by inverted tube observations. Hydrogels can form at the gelator concentration lower than 0.5 wt%, and the typical sample images are shown in Fig. 1. At a fixed SC concentration, phase transition from precipitates (P) to gels (G) then to P occurs with increasing amounts of C_nTAFB. With the addition of C_nTAFB, the hydrophobicity of the mixtures increases, weakening the gelation of the system and causing precipitates formation. As shown in Fig. 1, with an increase in hydrophobic chain length of C_nTAFB, the gel region decreases. C_nTAFC/SC system exhibits the same tendency (Fig. S2). For further detailed study, two series of sample were selected. One was at a fixed SC concentration of 50 $mmol{\cdot}L^{-1}$ with different amounts of C_nTAFB, whereas another was at a fixed molar ratio of SC to C_nTAFB being 2:1 with various total surfactant concentrations. The rheological properties, self-assembly process and

stimuli-response properties of the gels were illustrated by C_{12}TAFB/SC system.

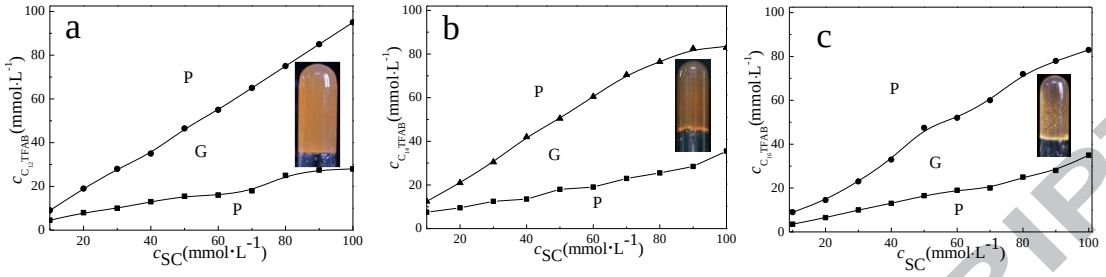

Fig. 1. Phase diagram of C_{12}TAFB/SC (a), C_{14}TAFB/SC (b), and C_{16}TAFB/SC (c) systems at 25.0 ± 0.1 ^{o}C.

3.2. Microstructure of hydrogels

TEM was employed to determine the microstructure in C_nTAFB/SC hydrogels. For TEM observations, a small amount of gels sample (without staining) was mounted onto the copper grid, and then freeze-dried for several days. From Fig. 2, a number of intertwined fibers with a width of 30 nm and the length of tens of micrometers were observed. These long fibers entangled with each other to form cross-linking networks, which immobilized water molecules through solvation and surface tension, resulting in the gelation [1]. At a fixed molar ratio of SC to C_{12}TAFB of 2:1, with the increase in total concentration, the diameter of the fibrils has no obvious change (Fig. 2a-d). With careful observation of Fig. 2c and d, one can find that with the increase in total concentration, a few bundles of fibrils are formed due to the increase in fibril density, which might be the reason of the opacity of the hydrogels at high concentration. Because the network of gels become more and more dense, and the structure are hardly observed, thus we do not give the microscopic images of the hydrogels at high gelator concentration.

The microstructure transition of another series of samples at a fixed SC concentration of 50 mmol·L^{-1} with different amounts of C_{12}TAFB was shown in Fig. 2c, e, f, and g. When the concentration of C_{12}TAFB is 20 mmol·L^{-1}, cross-linked

network fibrils with the diameter of about 30 nm can be found in Fig. 2e. With the increasing concentration of C_{12}TAFB, the density of fibril becomes more and more dense, leading to the formation of bundles of fibrils. When C_{12}TAFB concentration reaches 35 mmol·L^{-1}, lots of bundles of fibers are found, and the density of the fibers reaches a maximum value (Fig. 2f). When the concentration of C_{12}TAFB is above 35 mmol·L^{-1}, the density of fibers decreases. The probable reason may be that the continuously increasing of C_{12}TAFB concentration leads to the increase in the hydrophobicity of the mixtures, weakening the gelation and decreasing the density of fibers in gels. When the concentration is higher than 40 mmol·L^{-1}, only precipitates obtained. For C_{14}TAFB/SC and C_{16}TAFB/SC systems, the microstructure of the gels presents the similar tendency with that of C_{12}TAFB/SC system (Fig. S3 and S4), i.e., the density of fibers increases with increasing gelator concentration, and reaches a maximum value at the concentration of C_{14}TAFB (C_{16}TAFB) being 35 mmol·L^{-1}, then decreases with increasing of C_{14}TAFB (C_{16}TAFB) concentration.

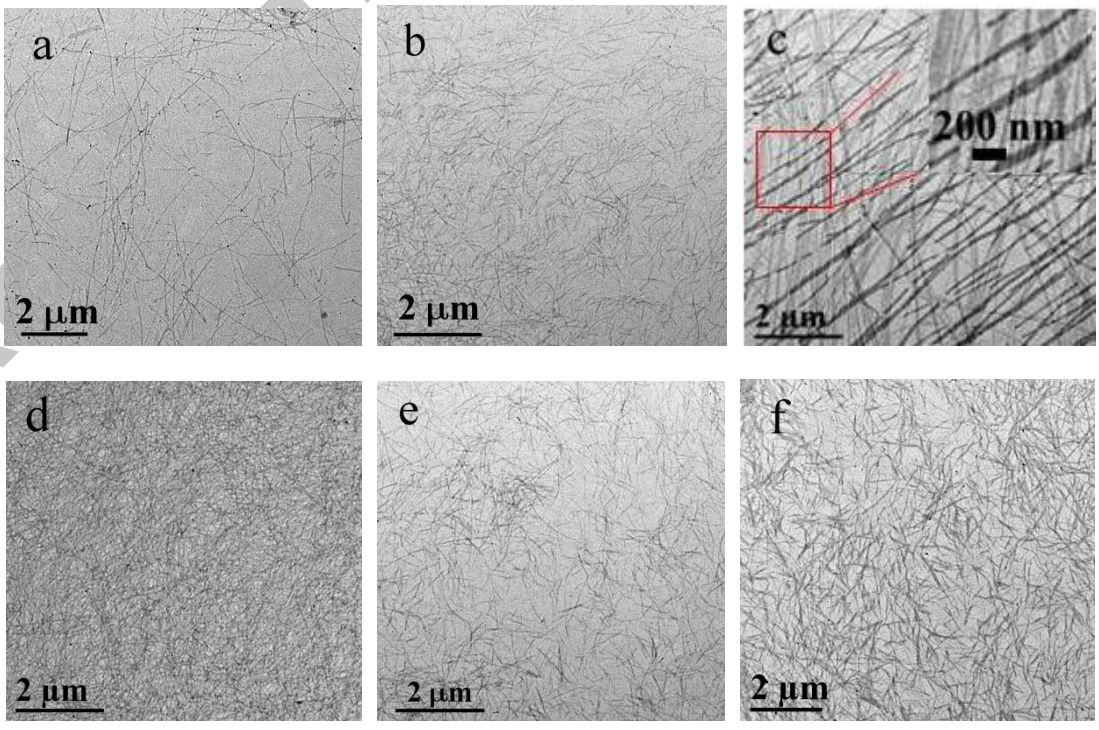

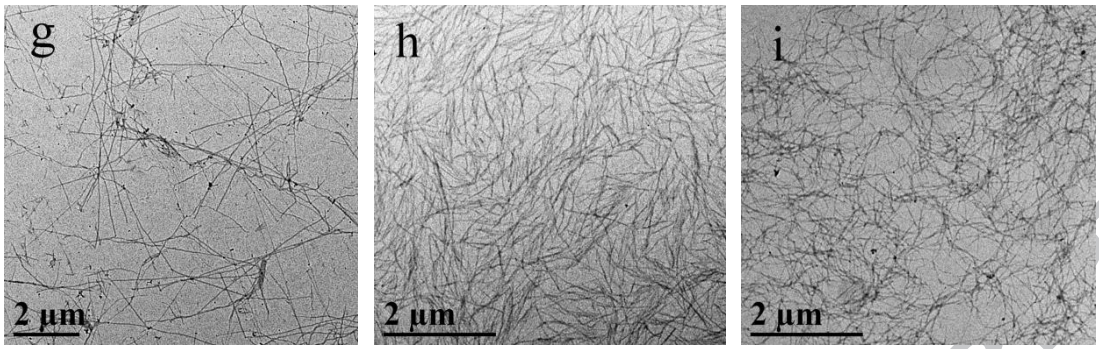

Fig. 2. TEM images of freeze-dried hydrogels formed by 20 mmol·L^{-1} SC/10 mmol·L^{-1} C_{12}TAFB (a), 40 mmol·L^{-1} SC/20 mmol·L^{-1} C_{12}TAFB (b), 50 mmol·L^{-1} SC/25 mmol·L^{-1} C_{12}TAFB (c), 60 mmol·L^{-1} SC/30 mmol·L^{-1} C_{12}TAFB (d), 50 mmol·L^{-1} SC/20 mmol·L^{-1} C_{12}TAFB (e), 50 mmol·L^{-1} SC/35 mmol·L^{-1} C_{12}TAFB (f), 50 mmol·L^{-1} SC/40 mmol·L^{-1} C_{12}TAFB (g), 50 mmol·L^{-1} SC/25 mmol·L^{-1} C_{14}TAFB (h), and 50 mmol·L^{-1} SC/25 mmol·L^{-1} C_{16}TAFB (i). An enlargement TEM image of hydrogels formed by 50 mmol·L^{-1} SC/25 mmol·L^{-1} C_{12}TAFB was inserted in (c).

3.3. Rheological property

To study the rheological property of hydrogels (e.g., viscoelasticity and mechanical strength) can not only provide parameters of materials to guide the applications but also supply different models to speculate the microstructures of materials [10]. The solid-like network structure of gels, when being sheared under an increasing stress, will break suddenly at a critical shear stress, τ*, beyond which a Newtonian-like flow occurs [1,51]. The critical shear stress (τ*) was called "yield stress", reflecting the strength of the network structures. We studied the influence of different factors on the mechanical strength of the hydrogels (Fig. 3). We firstly investigated the effect of the total concentration on the mechanical strength. At a fixed molar ratio of SC to C_{12}TAFB of 2:1, with the increase in total concentration, the yield stress increases gradually from 7 to 2000 Pa, which is ascribed to the more rigid network structure

induced by increasing of fibril density (Fig. 3a and e). For the sample of 100 mmol·L^{-1} SC/50 mmol·$L^{-1}$$C_{12}$TAFB (6.6 wt %), the yield stress can reach 2000 Pa, demonstrating the characteristic of soft viscoelastic solid [52,53]. The plateau value of the storage modus (*G'*) in the stress sweep can also be used to evaluate the mechanical strength of hydrogels. One can find that the *G'* value of the sample also rises with the total concentration, indicating the improvement of mechanical strength (Fig. 3e). The influence of C_{12}TAFB concentration on the mechanical strength was shown in Fig. 3b and f. At c_{SC} = 50 mmol·L^{-1}, with the increase in C_{12}TAFB concentration from 20 to 35 mmol·L^{-1}, the yield stress increases from 25 to 100 Pa, owing to the increase of fibril density. With further increase in C_{12}TAFB concentration, the yield stress decreases, indicating the decreasing in fibril density. One can find that the hydrogel formed at the concentration proportion of 50 mmol·L^{-1} SC to 35 mmol·L^{-1} C_{12}TAFB exhibit the highest mechanical strength, which illustrates that at this proportion the hydrogel possesses the densest fibers (Fig. 2f). The hydrophobic chain length of C_nTAFB has little influence on the mechanical strength of the gels. At the same concentration, C_{12}TAFB, C_{14}TAFB, and C_{16}TAFB systems almost have the same yield stress of about 100 Pa (Fig. 3c). Finally, the influence of anions on the mechanical strength was shown in Figure 3d. At the same concentration, the yield stress of C_{12}TAFB/SC system is much higher than that of C_{12}TAFC/SC system due to its higher gelation capability. Thus, we can conclude that the mechanical strength of the hydrogels can be regulated by changing the proportion of the two compounds, the concentration of the surfactants, and the sorts of anions.

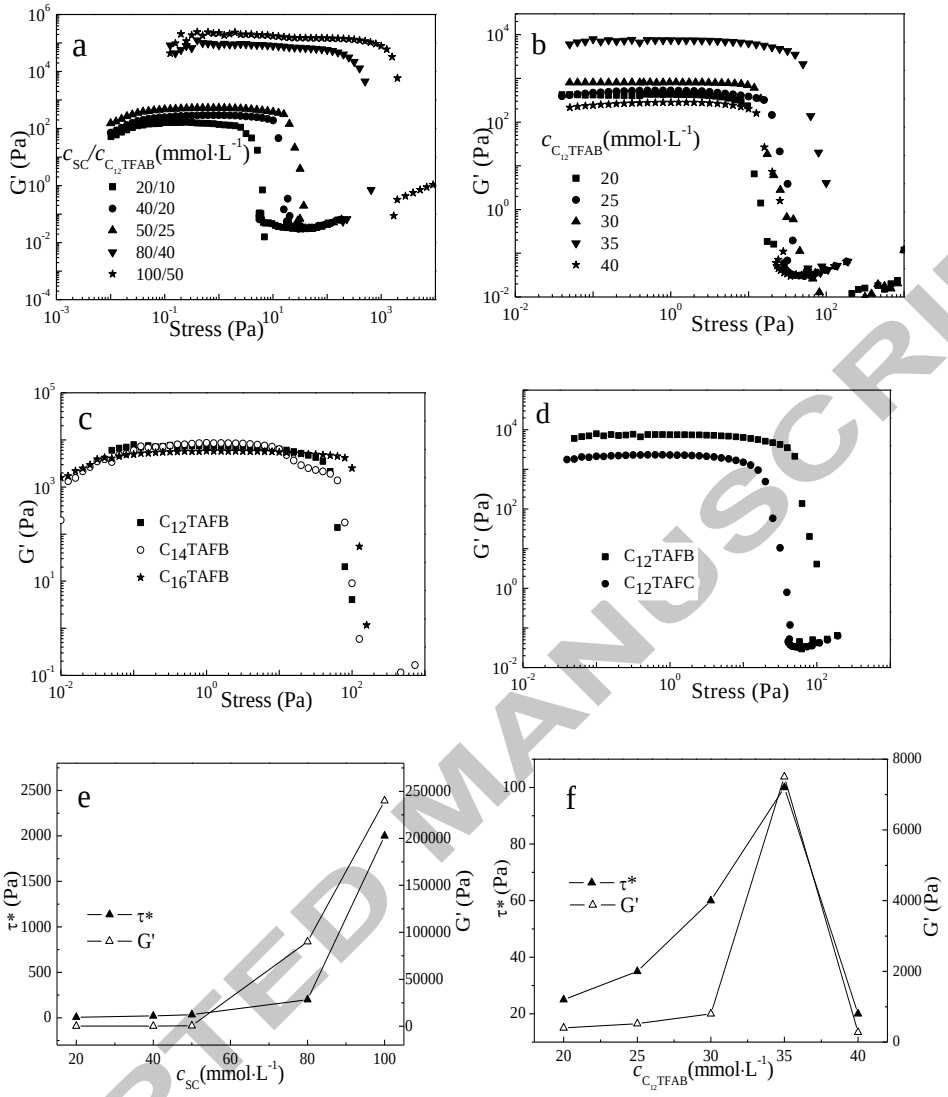

Fig. 3. G' as a function of oscillatory stress of hydrogels formed (a) at the molar ratio of SC to C_{12}TAFB of 2:1 with different total concentrations, (b) at c_{SC} = 50 mmol·L^{-1} with different amounts of C_{12}TAFB, (c) at the different chain length (50 mmol·L^{-1} SC/25 mmol·L^{-1} C_nTAFB), and (d) at 50 mmol·L^{-1} SC/25 mmol·L^{-1} C_{12}TAFB (C). (e) G' and τ* as the function of total concentration at the molar ratio of SC to C_{12}TAFB of 2:1, (f) G' and τ* as the function of C_{12}TAFB concentration.

Gels are viscoelastic soft solid-like materials that simultaneously store and display energy [4,53]. The viscoelasticity of gels can be characterized by two dynamic moduli: storage modulus (G'), which can estimate the degree of materials resistance against

mechanical disturbance, and loss modulus (G"), which measures the tendency of materials to flow under stress. Dynamic rheology was carried out to measure the viscoelasticity of C_{12}TAFB/SC hydrogels (Fig. 4). G' and G" are almost independent of the frequency over the studied frequency region and show an elastic dominant property, demonstrating a solid-like rheological behavior [54]. Expectedly, the absolute value of G' increases with the increase in total concentration at a fixed molar ratio of SC to C_{12}TAFB of 2:1 (Fig. 4a and b). At a fixed SC concentration of 50 mmol·L^{-1}, with an increase in C_{12}TAFB concentration, G' and G" increase firstly and then decrease (Fig. 4c and d). The stiffness/rigidity values of the hydrogels, i.e., the ratio of the dynamic moduli, G' and G", are found to be 4 to 10 (Tables S1 and S2), which further proved that with the increasing of total concentration, the fibers arranged more tightly, causing much higher mechanical strength.

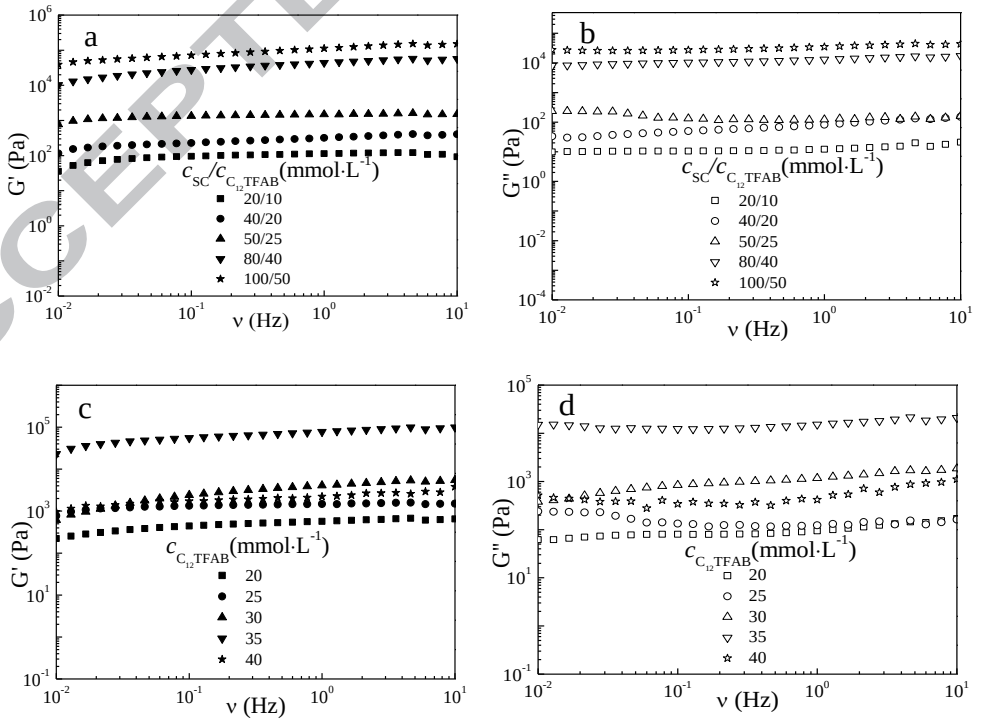

Fig. 4. G' (a) and G" (b) as a function of frequency for the molar ratio of SC to

C_{12}TAFB of 2:1 with different total concentrations; G' (c) and G" (d) as a function of frequency for 50 mmol·L^{-1}SC with different amounts of C_{12}TAFB.

3.4. Stimuli-responsive property

Hydrogels usually undergoes a gel-sol phase transition when temperature increases, which is accompanied by a reduction in the mechanical strength. For SC/C_{12}TAFB system, when extra energy (temperature or shearing force) was introduced, the hydrogels would experience a reversible gel-sol transition. As shown in Fig. S5, when being heated, the hydrogels can be converted into solution (sol) and the sol can be turned back to hydrogels upon cooling to R.T. for several hours. Moreover, the hydrogels can also be destroyed by shaking the sample vigorously to give a solution, and which can be recovered to hydrogels after being rested for 1 hour.

Differential scanning calorimetry (DSC) experiments were performed to detect the gel-sol transition temperature ($T_{gel\text{-}sol}$). An endothermic peak can be found in the heating curve, which indicates a positive enthalpy from gel to sol, as shown in Fig. 5. At a fixed molar ratio of SC to C_{12}TAFB of 2:1, with the increasing of total concentration, the endothermic peak shifts to a higher temperature, owing to the much denser network requires more energy to destroy the hydrogels (Fig. 5a and c). At c_{SC} = 50 mmol·L^{-1}, with the increasing C_{12}TAFB concentration from 20 to 35 mmol·L^{-1}, the $T_{gel-sol}$ increases from 31.86 to 72.73 ^{o}C firstly. With further increase in C_{12}TAFB amounts, $T_{gel-sol}$ decreases gradually. The $T_{gel-sol}$ variation tendency is consistent with the variation of mechanical strength of hydrogels.

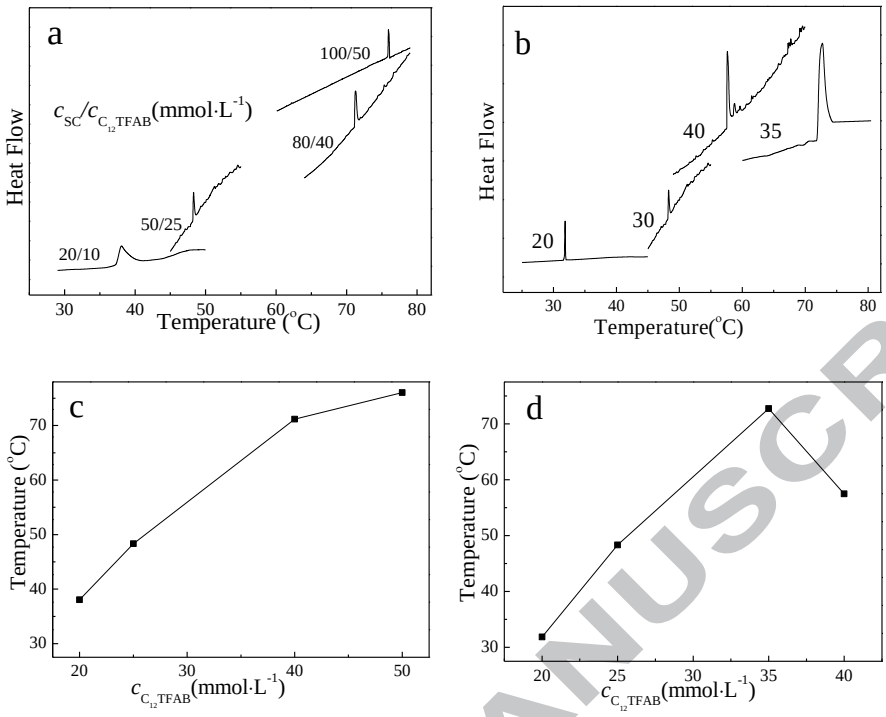

Fig. 5. (a) DSC curves of hydrogels formed by the molar ratio of SC to C_{12}TAFB of 2:1 with different total concentrations, (b) DSC curves of hydrogels formed by 50 mmol·L^{-1} SC with different amounts of C_{12}TAFB, (c) $T_{gel\text{-}sol}$ as a function of the total concentration, and (d) $T_{gel\text{-}sol}$ as a function of the concentration of C_{12}TAFB at c_{SC} = 50 mmol·L^{-1}.

3.5. Discussion

A proposal for the interaction between SC and C_{12}TAFB for the formation of fibrous structures in hydrogels was shown in Scheme 1. When SC was added to C_{12}TAFB solution, $C_{12}TA^{+}$…cholate ion pairs would be formed due to the electrostatic interaction. SC is a facial amphiphile with several chiral centers and a rigid steroid skeleton. Three hydroxyl groups and a carboxyl group are oriented to the concave side of the rigid steroid ring, being rendered hydrophilic, while the convex side is hydrophobic [12]. As shown in Scheme 1, hydrogen bonding exists between

the two reversed SC hydroxyl groups. Each SC molecule connects with another reversed SC molecule through hydrogen bonding and a C_nTAFB molecule through electrostatic interaction. Driven by hydrophobic interaction, electrostatic interaction, hydrogen bonding, and van der Waals force, the arrays combine with each other. Due to the rigid steroid skeleton and the chiral structure of SC molecules, the arrays cannot extend in linearity, but tilt to induce the formation of fibers.

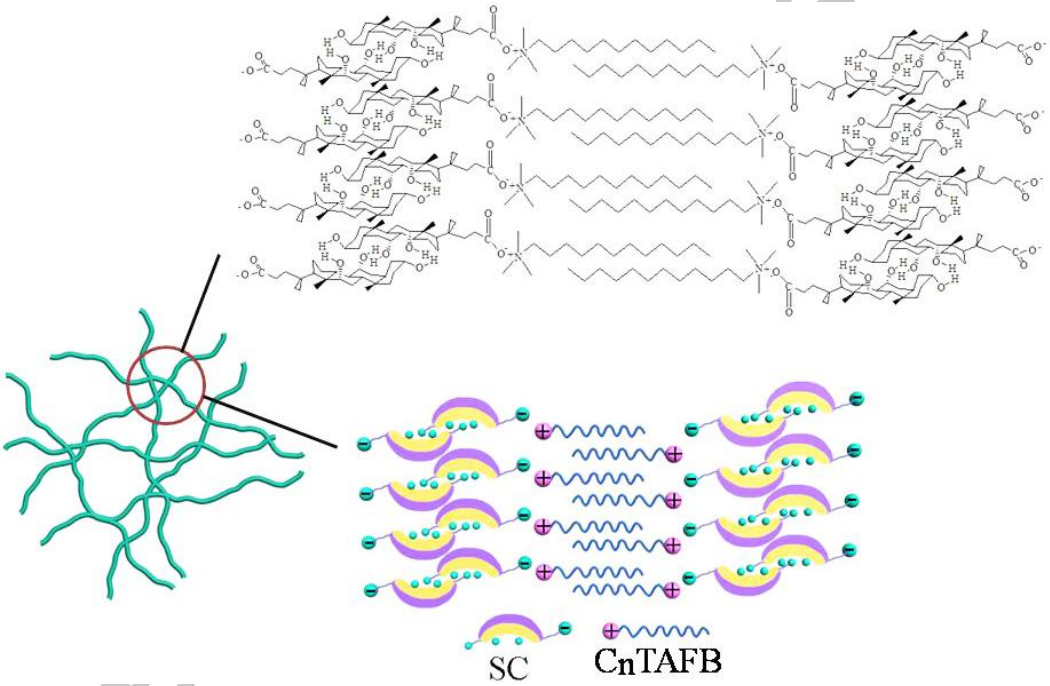

Scheme 1. Proposed mechanism of fibrils formed in SC/C_nTAFB hydrogels.

FT-IR and small-angle X-ray diffraction (SXRD) experiments were performed to support the proposed mechanism of the formation of fibrils in hydrogels. The FT-IR spectra in Fig. S6 (curves b - d) within the wavelength region of 3000–4000 cm^{-1} demonstrated the hydrogen bonding between the hydroxyl groups of two reversed SC molecules. The arrangement of C_nTAFB and SC molecules in hydrogels was revealed by SXRD patterns (Fig. 6). According to Bragg's law, the three well-resolved reflection peaks at 3.35, 4.56, and 7.65^o were calculated corresponding to the d

spacing of 2.65, 1.94, and 1.15 nm, respectively, which were considered to relate to some cycled units of the arrangements formed by SC and C_{12}TAFB. The d value of 2.65 nm is just a little less than the twice of the chain length of C_{12}TAFB molecule (1.672 nm) [50], belonging to the combination of two C_{12}TAFB molecules through hydrophobic interaction in each unit of the arrays. The d value of 1.93 nm is just a little longer than a cholate backbone length (1.5 nm), which might be ascribed to the elongation induced by the side-by-side connection of two reversed SC molecules in each unit through intermolecular hydrogen bonding [54-58]. The distance of 1.15 nm is comparable with twice the thickness of cholate skeleton (0.6 nm × 2) [54]. The position of the reflection peaks was almost unchanged with the variation of concentration or proportion of SC and C_{12}TAFB, demonstrating the same molecular arrangement in the fibers of hydrogel.

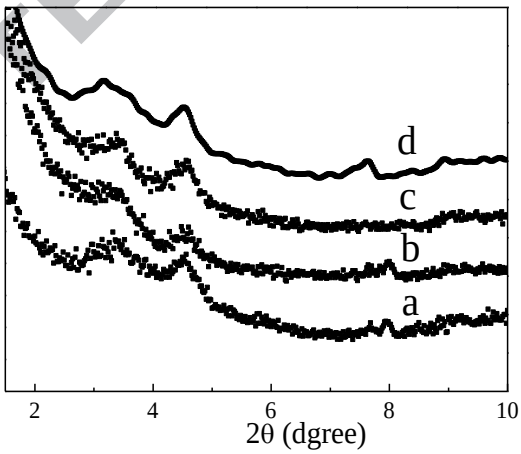

Fig. 6. SXRD patterns of dried hydrogels formed by (a) 20 mmol·L^{-1} SC/10 mmol·L^{-1} C_{12}TAFB, (b) 50 mmol·L^{-1} SC/20 mmol·L^{-1} C_{12}TAFB, (c) 50 mmol·L^{-1} SC/25 mmol·L^{-1} C_{12}TAFB, and (d) 50 mmol·L^{-1} SC/35 mmol·L^{-1} C_{12}TAFB.

3.6. Hydrogel as precursors for producing Fe_3O_4 MNPs

As a representative demonstration, the preparation of Fe_3O_4 MNPs based on

SC/C_{12}TAFB hydrogels with NaOH as the precipitator will be discussed in detail. Cationic surfactant (C_{12}TAFB) has larger anion, $[FeCl_3Br]^-$, which can gradually release Fe^{3+}. SC/C_{12}TAFB hydrogels loaded with Fe^{2+} were added into NaOH aqueous solution. After being kept at 50 ^oC in water bath for 12 h, black Fe_3O_4 precipitates were obtained. The XRD pattern of the obtained Fe_3O_4 precipitates (Fig. 7a) could be indexed to cubic phase (space group Fd3m, no.227), which was in good accordance with the ICPDS file of Fe_3O_4 (JCPDS NO.65-3107). From the TEM image in Fig. 7b, it is clearly observed that the obtained Fe_3O_4 possess cubic geometrical morphology with an average edge length of 7.2 nm. The selected-area electron diffraction (SAED) pattern (Fig. 7c) is consistent with the XRD pattern. Well resolved 2D lattice fringes with a lattice spacing of 0.245 nm are observed in the high-resolution transmission electron microscopy (HR-TEM) image (Fig. 7d), which is in compliance with the (2,2,2) crystalline plane of the cubic Fe_3O_4. The magnetic properties of the cubic Fe_3O_4 were studied with a superconducting quantum interferometer device (SQUID) magnetometer from Quantum Design. The hysteresis loop of cubic Fe_3O_4 in low filed from -400 Oe to 400 Oe exhibits clear ferromagnetic characteristics with saturation magnetization, remanent magnetization and coercivity of 62 $emug \cdot g^{-1}$, 0.85 $emug \cdot g^{-1}$ and 17 Oe, respectively (Fig. 7e). Owing to the excellent viscoelastic of hydrogels and the existence of $[FeCl_3Br]^-$, SC/C_{12}TAFB hydrogel is a good precursor for preparing Fe_3O_4MNPs. The simple method was carried out under mild conditions in aqueous solution, eliminating the use of complex and toxic organometallic reactants as well as the complicated process and high

temperature required in common Fe_3O_4 preparation [37].

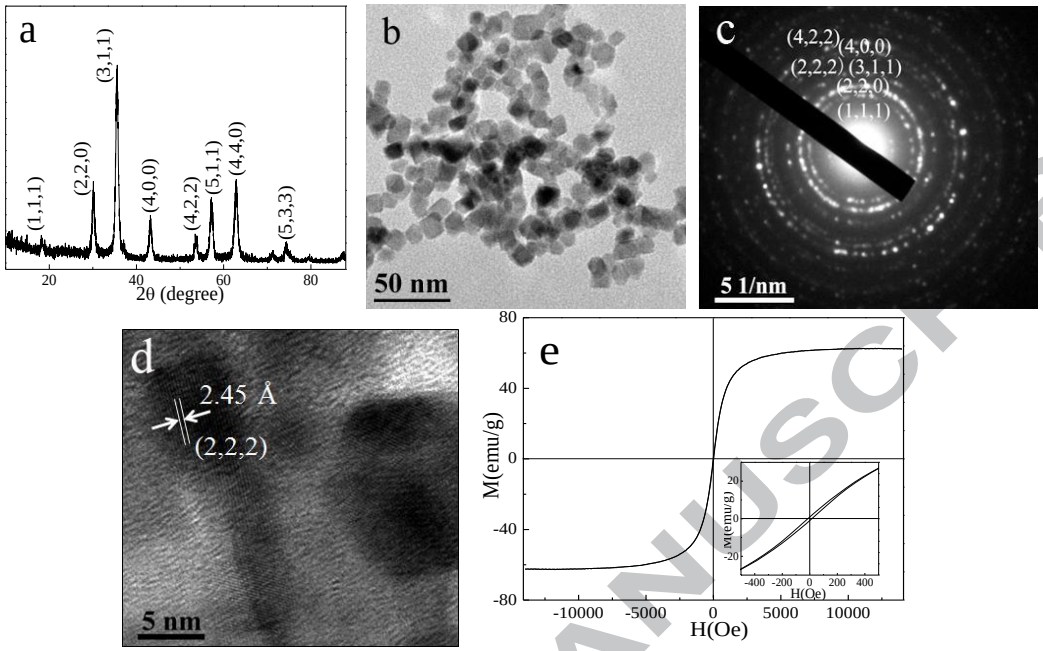

Fig. 7. a) XRD pattern, b) TEM image, c) SAED pattern, d) HR-TEM image, e) SQUID magnetometry of Fe_3O_4 MNPs prepared from SC/C_{12}TAFB hydrogels.

3.7. Fe_3O_4 MNPs catalyses the oxidation of peroxidase substrates

Fe_3O_4 MNPs are usually considered chemically and biologically inert, which has been widely used for bioanalysis, bioelectrocatalysis, drug delivery, bacteria inactivation, etc [59,60]. According to the literature, Fe_3O_4 MNPs within the size range of 5-7 nm have a greater surface-to-volume ratio to interact with substrates and exhibit higher peroxidase-like activity [59,60]. To investigate the catalytic activity of Fe_3O_4 MNPs, the catalytic oxidation process of the peroxidase substrate, 3,3',5,5'-tetramethylbenzidine (TMB), in the presence of H_2O_2 was tested. As shown in Fig. 8a (curve 1), Fe_3O_4 MNPs can catalyze the oxidation of TMB in the presence of H_2O_2 to produce a blue color reaction, which exhibits a maximum absorbance at 652 nm. In the absence of Fe_3O_4 MNPs or TMB, the colorless solution showed a negligible absorption in the range of 450 to 800 nm (curves 3 and 4). Notably, the obtained Fe_3O_4 MNPs with the average size of 7.2 nm present much higher catalytic

activity than HRP at the same condition (curves 1 and 2) due to its higher surface-to-volume ratio.

In order to interpret the reaction mechanism of the peroxidase activity of the Fe_3O_4 MNPs, the apparent steady-state kinetic parameters for the reaction were measured. Typical Michaelis-Menten curves were observed for Fe_3O_4 MNPs with TMB or H_2O_2 as substrates (Fig. 8b and c). The Lineweaver-Burk plot method was used to investigate whether the catalytic reaction of Fe_3O_4 MNPs followed the Michaelis-Menten behavior. As shown in Figure 8d and e, the reciprocal of the initial rate was directly proportional to the substrate concentration. The double reciprocal plots of the Michaelis-Menten equation were applied to obtain the catalytic parameters, as shown in Table 2. The apparent K_m value of the obtained Fe_3O_4 MNPs was significantly lower than that for HRP towards H_2O_2 and TMB [27,36], indicating that the obtained Fe_3O_4 MNPs had a higher affinity to TMB and H_2O_2 than HRP. Compared with the reported nanomaterial with peroxidase-like activities such as FeS, $ZnFe_2O_4$, and Au-Pt, the obtained Fe_3O_4 MNPs had the smallest K_m value, which should be attributed to its small size and unique cubic structure [31-34].

Table 2 Michaelis constant (K_m) and maximal reaction rate (V_{max}) of Fe_3O_4 MNPs.

catalyst	substrate	K_m(mmol·L^{-1})	V_{max} (10^{-8} mol·L^{-1}·s^{-1})
Fe_3O_4 MNPs	TMB	0.091	5.18
	H_2O_2	0.01957	1.26
HRP	TMB [27]	0.434	10.0
	H_2O_2 [27]	3.70	8.71

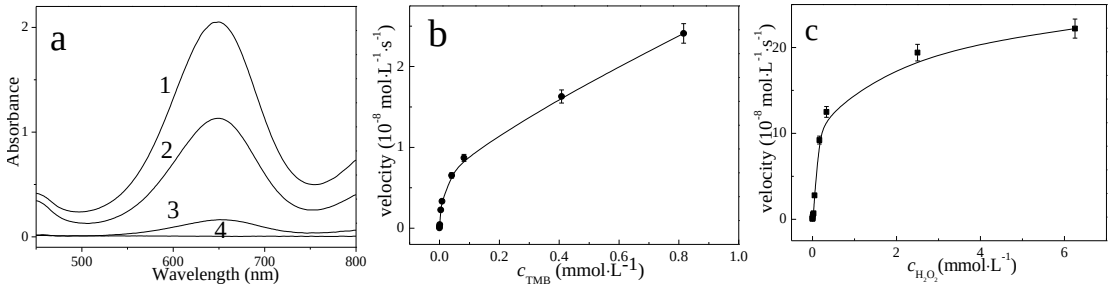

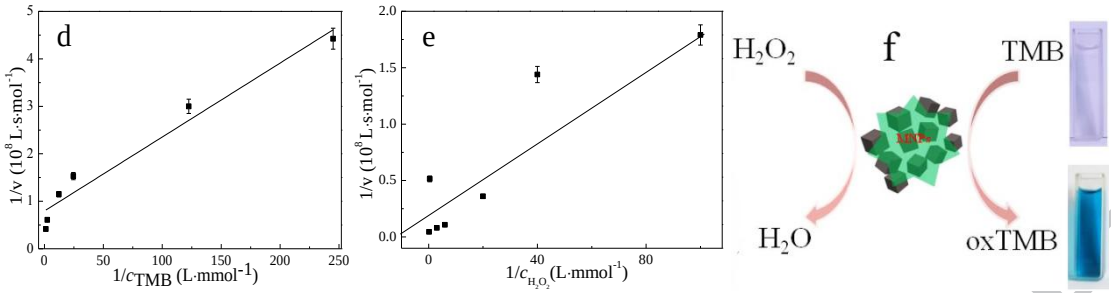

Fig. 8. (a) Typical absorption spectra of aqueous suspensions of the corresponding reactions incubated at 40 ^{o}C in acetate buffer (8 mL, 0.2 mol·L^{-1}, pH = 4.0), curve 1: 50 μg Fe_3O_4 MNPs with 816 μmol·L^{-1} TMB and 10 mmol·L^{-1} H_2O_2; curve 2: 1 ng HRP with 816 μmol·L^{-1} TMB and 10 mmol·L^{-1} H_2O_2; curve 3: 816 μmol·L^{-1} TMB and 10 mmol·L^{-1} H_2O_2 without Fe_3O_4 MNPs; and curve 4: 50 μg Fe_3O_4 MNPs and 10 mmol·L^{-1} H_2O_2 without TMB. (b-e) Steady-state kinetic assay and catalytic mechanism of Fe_3O_4 MNPs. The velocity (*v*) of the reaction was measured using 50 μg Fe_3O_4 MNPs in acetate buffer (8 mL, 0.2 mol·L^{-1}, pH = 4.0) at 40 ^{o}C (b,c). The concentration of H_2O_2 was 10 mmol·L^{-1} and the TMB concentration was varied (b,d). The concentration of TMB was 816 μmmol·L^{-1} and the H_2O_2 concentration was varied (c,e). Schematic illustration of colorimetric determination of H_2O_2 using Fe_3O_4 MNPs catalyzed reactions (f).

As shown in Fig. S7a and b, the peroxidase-like activity of the Fe_3O_4 MNPs is inhibited at higher H_2O_2 concentrations. However, within the concentration range of H_2O_2 from 1 to 10 μmol·L^{-1}, the absorbance at 652 nm versus the concentration of H_2O_2 presents good linearity with a correlation coefficient of 0.99954 (Fig. 9a and b), which indicates that the change of the absorbance at 652 nm can be used for H_2O_2 detection. The detection limit for H_2O_2 is calculated to be 0.1 μmol·L^{-1} (3σ/K), being better than that of other Fe_3O_4 and Au nanoparticles [36,37,60]. The images of color reaction of TMB with different concentrations of H_2O_2 were shown in Fig. S7c.

3.8. Glucose detection

Since H_2O_2 is the product of glucose oxidation reaction by glucose oxidase (GOx), we established a colorimetric biosensor for glucose detection when Fe_3O_4 MNPs was coupled with the glucose catalytic reaction (Fig. 9f). Fig. 9c and d show the calibration curve for glucose detection under conventional condition. The linear response (R = 0.9998) of the absorbance at 652 nm versus glucose concentration is within the range of 1.0 - 40 μmol·L^{-1}. The detection limit of glucose is 0.37 μmol·L^{-1} (3σ/K). To examine the selectivity of glucose detection, control experiments were carried out using 10 mmol·L^{-1} lactose, 10 mmol·L^{-1} fructose, and 10 mmol·L^{-1} maltose in replacement of glucose (38.5 μmol·L^{-1}). No detectable signals were observed (Fig. 9e). Thus, the proposed biosensor system is highly sensitive for glucose detection. Due to the observable change from colorless to blue by naked eyes, the visual detection can be realized without any instruments or complicated designs, which hopefully to be a novel candidate glucose sensor for glucose detection.

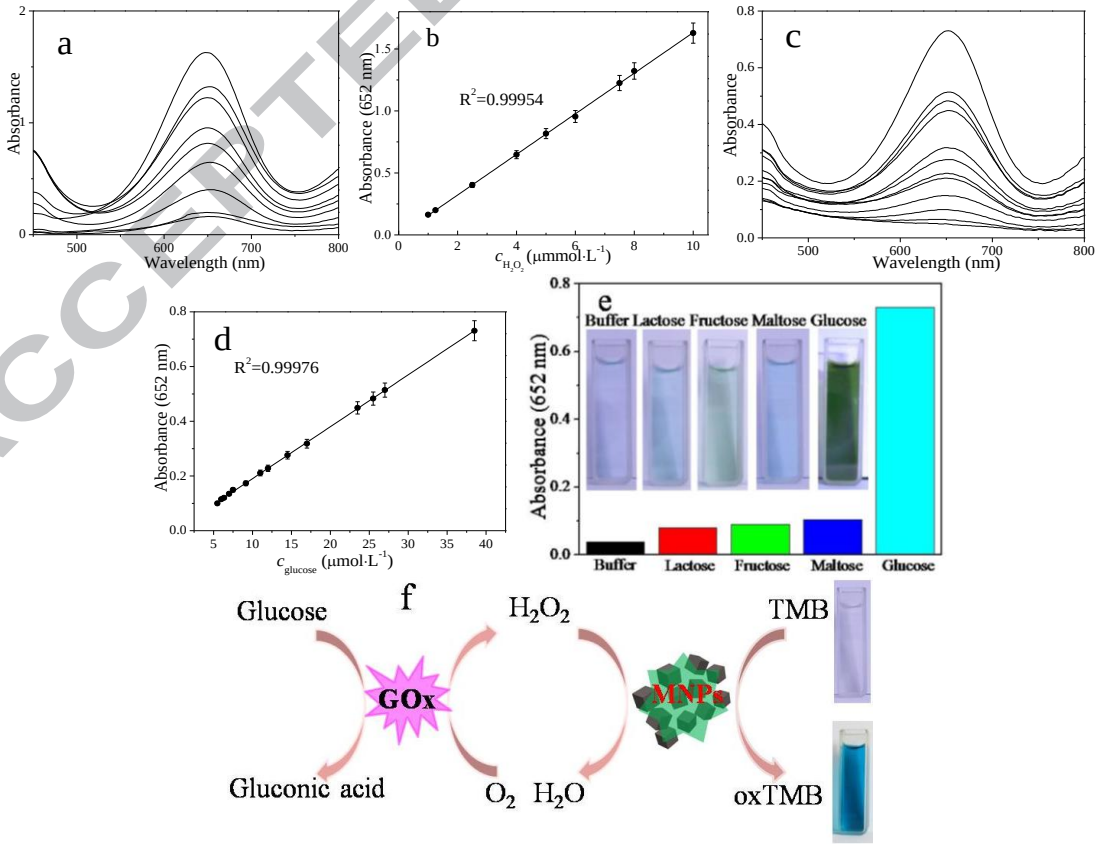

Fig. 9. H_2O_2 and glucose detection based on Fe_3O_4 MNPs. The UV-vis spectra of (a)

H_2O_2 solution and (c) glucose solution with Fe_3O_4 MNPs and 816 μmol·L^{-1} TMB in acetate buffer (pH = 4.0). The concentration of H_2O_2 (μmol·L^{-1}) in (a) from top to bottom is 10, 8, 7.5, 6, 5, 4, 2.5, 1.25, and 1. The concentration of glucose (μmol·L^{-1}) in (c) from top to bottom is 38.5, 27, 25.5, 23.5, 17, 14.5, 12, 11, 7.5, 5.5, 0.00143, and 0.00016. The linear calibration plot for H_2O_2 (b) and glucose (d). Selectivity analysis for glucose detection by monitoring the absorbance at 652 nm (e), the analyte concentration were as follows: 10 mmol·L^{-1} lactose, 10 mmol·L^{-1} fructose, 10 mmol·L^{-1} maltose, and 38.5 μmol·L^{-1} glucose, inset: the color change with the different solutions. Schematic illustration of colorimetric determination of glucose using glucose (GOx) and Fe_3O_4 MNPs catalyzed reactions (f).

4. Conclusions

In summary, stimuli-response magnetic hydrogels with excellent mechanical strength were obtained by mixing the magnetic surfactant, C_nTAFB(C) (n = 12, 14, 16), and SC in water. The gelation behavior of C_nTAFB(C)/SC systems indicated that the hydrophobic interaction and R_h of anions play significant roles in gelation process. The microstructure of hydrogels was observed to be nanofibrils with a width of 30 nm and the length of tens of micrometers. The increase in total concentration triggered the increase in the density of the fibers, corresponding to the mechanical strength enhancement and the $T_{gel-sol}$ elevating. C_{12}TAFB/SC hydrogels served as the precursor for preparing cubic Fe_3O_4 nanoparticles with excellent ferromagnetic characteristics and higher peroxidase-like activity, which could be used as biosensor for H_2O_2 and glucose detection, expanding the range of biosensor platform used for biological assay. We hope our results will promote the further theoretical study on designing amphiphiles hydrogels, and provide a wide range of applications for Fe_3O_4 nanoparticles mimetic enzyme systems in bio-detection, catalysis, and clinical

diagnostics.

Acknowledgements

This work is financially supported by the NSFC (21603123), the Opening Project of Oil & Gas Field Applied Chemistry Key Laboratory of Sichuan Province (KF201405).

References

[1] S. Song, L. Feng, A. Song, J. Hao, Room-temperature super hydrogel as dye adsorption agent, J. Phys. Chem. B 116 (2012) 12850–12856.

[2] G. Yu, X. Yan, C. Han, F. Huang, Characterization of supramolecular gels, Chem. Soc. Rev. 42 (2013) 6697–6722.

[3] J. Steed, Anion-tuned supramolecular gels: a natural evolution from urea supramolecular chemistry, Chem. Soc. Rev. 39 (2010) 3686–3699.

[4] A. Pal, H. Basit, S. Sen, V. Aswal, S. Bhattacharya, Structure and properties of two component hydrogels comprising lithocholic acid and organic amines, J. Mater. Chem. 19 (2009) 4325–4334.

[5] Y. Qiao, Y. Lin, S. Zhang, J. Huang, Lanthanide - containing photoluminescent materials: from hybrid hydrogel to inorganic nanotubes, Chem. Eur. J. 17 (2011) 5180–5187.

[6] A. Ajayaghosh, S. George, V. Praveen, Gelation-assisted light harvesting by selective energy transfer from an oligo (p - phenylenevinylene) ‐ based self ‐ assembly to an organic dye, Angew. Chem. Int. Ed. 42 (2003) 332–335.

[7] D. Wang, G. Wei, R. Dong, J. Hao, Multiresponsive viscoelastic vesicle gels of

nonionic $C_{12}EO_4$ and anionic AzoNa, Chem. Eur. J. 19 (2013) 8253–8260.

[8] H. Wang, S. Song, J. Hao, A. Song, Hydrogels triggered by metal ions as precursors of network CuS for DNA detection, Chem. Eur. J. 21 (2015) 12194–12201.

[9] L. Buerklea, S. Rowan, Supramolecular gels formed from multi-component low molecular weight species, Chem. Soc. Rev. 41 (2012) 6089–6102.

[10] S. Song, A. Song, L. Feng, G. Wei, S. Dong, J. Hao, Fluorescent hydrogels with tunable nanostructure and viscoelasticity for formaldehyde removal, ACS Appl. Mater. Interfaces 6 (2014) 18319−18328.

[11] J. Lehn, Perspectives in chemistry-steps towards complex matter, Angew. Chem. Int. Ed. 52 (2013) 2836 –2850.

[12] D. Madenci, S. Egelhaaf, Self-assembly in aqueous bile salt solutions, Curr. Opin. Colloid Interface Sci. 15 (2010) 109–115.

[13] P. Terech, A. Geyer, B. Struth, Y. Talmon, Self-assembled monodisperse steroid nanotubes in water, Adv. Mater. 14 (2002) 495−498.

[14] X. Zhang, J. Zou, K. Tamhane, F. Kobzeff, J. Fang, Self-assembly of pH‐switchable spiral tubes: supramolecular chemical springs, Small 6 (2010) 217−220.

[15] M. Gubitosi, L. Travaglini, M. Gregorio, N. Pavel, J. Tato, S. Sennato, U. Olsson, K. Schillén, L. Galantini, Tailoring supramolecular nanotubes by bile salt based surfactant mixtures, Angew. Chem. Int. Ed. 54 (2015) 7018 –7021.

[16] B. Jean, L. Oss-Ronen, P. Terech, Y. Talmon, Monodisperse bile-salt nanotubes

in water: kinetics of formation, Adv. Mater. 17 (2005) 728–731.

[17] P. Terech, B. Jean, F. Ne, Hexagonally ordered ammonium lithocholate self-sssembled nanotubes with highly monodisperse sections, Adv. Mater. 18 (2006) 1571–1574.

[18] P. Terech, N. Sangeetha, S. Bhat, J. Allegraud, E. Buhler, Ammonium lithocholate nanotubes: stability and copper metallization, Soft Matter 2 (2006) 517–522.

[19] P. Dastidar, S. Okabe, K. Nakano, K. Iida, M. Miyata, N. Tohnai, M. Shibayama, Facile syntheses of a class of supramolecular gelator following a combinatorial library approach: dynamic light scattering and small-angle neutron scattering studies, Chem. Mater. 17 (2005) 741–748.

[20] Y. Qiao, Y. Lin, Y. Wang, Z. Yang, J. Liu, J. Zhou, Y. Yan, J. Huang, Metal-driven hierarchical self-assembled one-dimensional nanohelices, Nano Lett. 9 (2009) 4500−4504.

[21] N. Li, Y. Yan, B. Xia, J. Wang, X. Wang, Novel tungsten carbide nanorods: an intrinsic peroxidase mimetic with high activity and stability in aqueous and organic solvents, Biosens. Bioelectron. 54 (2014) 521–527.

[22] Y. Chen, H. Cao, W. Shi, H. Liu, Y. Huang, Fe–Co bimetallic alloy nanoparticles as a highly active peroxidase mimetic and its application in biosensing, Chem. Commun. 49 (2013) 5013–5015.

[23] Y. Long, Y. Li, Y. Liu, J. Zheng, J. Tang, C. Huang, Visual observation of the mercury-stimulated peroxidase mimetic activity of gold nanoparticles, Chem.

Commun. 47 (2011) 11939–11941.

[24] J. Liu, X. Hu, S. Hou, T. Wen, W. Liu, X. Zhu, X. Wu, Screening of inhibitors for oxidase mimics of Au@Pt nanorods by catalytic oxidation of OPD, Chem. Commun. 47 (2011) 10981–10983.

[25] M. Wiester, P. Ulmann, C. Mirkin, Enzyme mimics based upon supramolecular coordination chemistry, Angew. Chem. Int. Ed. 50 (2011) 114–137.

[26] R. Schirhagl, D. Podlipna, P. Lieberzeit, F. Dickert, Comparing biomimetic and biological receptors for insulin sensing. Chem. Commun. 46 (2010) 3128–3130.

[27] L. Gao, J. Zhuang, L. Nie, J. Zhang, Y. Zhang, N. Gu, T. Wang, J. Feng, D. Yang, S. Perrett, X. Yan, Intrinsic peroxidase-like activity of ferromagnetic nanoparticles, Nat. Nanotechnol. 2 (2007) 577–583.

[28] Y. Song, K. Qu, C. Zhao, J. Ren, X. Qu, Graphene oxide: intrinsic peroxidase catalytic activity and its application to glucose detection, Adv. Mater. 22 (2010) 2206–2210.

[29] Y. Song, X. Wang, C. Zhao, K. Qu, J. Ren, X. Qu, Label-free colorimetric detection of single nucleotide polymorphism by using single-walled carbon nanotube intrinsic peroxidase-like activity, Chem. Eur. J. 16 (2010) 3617–3621.

[30] W. Shi, Q. Wang, Y. Long, Z. Cheng, S. Chen, H. Zheng, Y. Huang, Carbon nanodots as peroxidase mimetics and their applications to glucose detection, Chem. Commun. 47 (2011) 6695–6697.

[31] W. He, X. Wu, J. Liu, X. Hu, K. Zhang, S. Hou, W. Zhou, S. Xie, Design of AgM bimetallic alloy nanostructures (M= Au, Pd, Pt) with tunable morphology and

peroxidase-like activity, Chem. Mater. 22 (2010) 2988–2994.

[32] T. Pirmohamed, J. Dowding, S. Singh, B. Wasserman, E. Heckert, A. Karakoti, J. King, S. Seal, W. Self, Nanoceria exhibit redox state-dependent catalase mimetic activity, Chem. Commun. 46 (2010) 2736–2738.

[33] Z. Dai, S. Liu, J. Bao, H. Ju, Nanostructured FeS as a mimic peroxidase for biocatalysis and biosensing, Chem. Eur. J. 15 (2009) 4321–4326.

[34] Y. Jv, B. Li, R. Cao, Positively-charged gold nanoparticles as peroxidiase mimic and their application in hydrogen peroxide and glucose detection, Chem. Commun. 46 (2010) 8017–8019.

[35] Z. Wang, H. Liu, S. Yang, T. Wang, C. Liu, Y. Cao, Nanoparticle-based artificial RNA silencing machinery for antiviral therapy, Proc. Natl. Acad. Sci. 109 (2012) 12387–12392.

[36] X. Jiang, C. Sun, Y. Guo, G. Nie, L. Xu, Peroxidase-like activity of apoferritin paired gold clusters for glucose detection, Biosens. Bioelectron. 64 (2015) 165–170.

[37] Y. Gao, Z. Wei, F. Li, Z. Yang, Y. Chen, M. Zrinyi, Y. Osada, Synthesis of a morphology controllable Fe_3O_4 nanoparticle/hydrogel magnetic nanocomposite inspired by magnetotactic bacteria and its application in H_2O_2 detection, Green Chem. 16 (2014) 1255–1261.

[38] S. Liu, F. Lu, R. Xing, J. Zhu, Structural effects of Fe_3O_4 nanocrystals on peroxidase-like activity, Chem. Eur. J. 17 (2011) 620–625.

[39] H. Qi, Q. Chen, M. Wang, M. Wen, J. Xiong, Study of self-assembly of

octahedral magnetite under an external magnetic field, J. Phys. Chem. C 113 (2009) 17301–17305.

[40] P. Brown, A. Bushmelev, C. Butts, J. Cheng, J. Eastoe, I. Grillo, R. Heenan, A. Schmidt, Magnetic control over liquid surface properties with responsive surfactants, Angew. Chem. Int. Ed. 51 (2012) 2414–2416.

[41] P. Brown, A. Bushmelev, C. Butts, J. Cheng, J. Eastoe, C. Russell, G. Smith, Magnetic emulsions with responsive surfactants, Soft Matter 8 (2012) 3545–3546.

[42] P. Brown, A. Kahn, J. Armstrong, A. Perriman, C. Butts, J. Eastoe, Magnetizing DNA and proteins using responsive surfactants, Adv. Mater. 24 (2012) 6244–6247.

[43] A. Ghosh, J. Dey, pH-Responsive and thermoreversible hydrogels of N-(2-hydroxyalkyl)-l-valine amphiphiles, Langmuir 25 (2009) 8466–8472.

[44] S. Song, R. Dong, D. Wang, A. Song, J. Hao, Temperature regulated supramolecular structures *via* modifying the balance of multiple non-covalent interactions, Soft Matter 9 (2013) 4209−4218.

[45] F. Menger, K. Caran, Amino acid derivatives that rigidify water at submillimolar concentrations, J. Am. Chem. Soc. 122 (2000) 11679–11691.

[46] L. Estroffand, A. Hamilton, Water gelation by small organic molecules, Chem. Rev. 104 (2004) 1201–1217.

[47] T. Becker, C. Goh, F. Jones, M. McIIdowie, Proline-functionalised calix[4]arene: an anion-triggered hydrogelator. Chem. Commun. 2008, 3900–3902.

[48] D. Abdallah, R. Weiss, The influence of the cationic center, anion, and chain length of tetra-*n*-alkylammonium and -phosphonium salt gelators on the properties of their thermally reversible organogels, Chem. Mater. 12 (2000) 406–413.

[49] S. Flores, S. Kherb, N. Konelick, X. Chen, P. Cremer, The effects of hofmeister cations at negatively charged hydrophilic surfaces, J. Phys. Chem. C 116 (2012) 5730–5734.

[50] O. Regev, F. Guillemet, Various bilayer organizations in a single-tail nonionic surfactant: unilamellar vesicles, multilamellar vesicles, and flat-stacked lamellae, Langmuir 15 (1999) 15, 4357–4364.

[51] P. Terech, S. Dourdain, U. Maitra, S. Bhat, Structure and rheology of cationic molecular hydrogels of quinuclidine grafted bile salts. Influence of the ionic strength and counter-ion type, J. Phys. Chem. B 113 (2009) 4619−4630.

[52] P. Cordier, F. Tournilhac, C. Soulié-Ziakovic, L. Leibler, Self-healing and thermoreversible rubber from supramolecular assembly, Nature 451 (2008) 977−980.

[53] Y. Hisamatsu, S. Banerjee, M. Avinash, T. Govindaraju, C. Schmuck, A supramolecular gel from a quadruple zwitterion that responds to both acid and base, Angew. Chem. Int. Ed. 52 (2013) 12550−12554.

[54] L. Jiang, Y. Yan, J. Huang, Zwitterionic surfactant/cyclodextrin hydrogel: microtubes and multiple responses, Soft Matter 7 (2011) 10417−10423.

[55] L. Schefer, A. Sánchez-Ferrer, J. Adamcik, R. Mezzenga, Resolving

self-assembly of bile acids at the molecular length scale, Langmuir 28 (2012) 5999–6005.

[56] F. Garczarek, K. Gerwert, Functional waters in intraprotein proton transfer monitored by FTIR difference spectroscopy, Nature 439 (2006) 109–112.

[57] A. Kasal, M. Budesinsky, W. Griffiths, Spectroscopic methods of steroid analysis, Steroid Analysis, 2nd ed., Springer, Netherlands, 2010, 27–161.

[58] S. Song, H. Wang, A. Song, J. Hao, Superhydrogels of nanotubes capable of capturing heavy-metal ions, Chem. Asian J. 9 (2014) 245–252.

[59] H. Wei, E. Wang, Nanomaterials with enzyme-like characteristics (nanozymes): next-generation artificial enzymes, Chem. Soc. Rev. 42 (2013) 6060–6093.

[60] H. Wei, E. Wang, Fe_3O_4 magnetic nanoparticles as peroxidase mimetics and their applications in H_2O_2 and glucose detection, Anal. Chem. 80 (2008) 2250–2254.

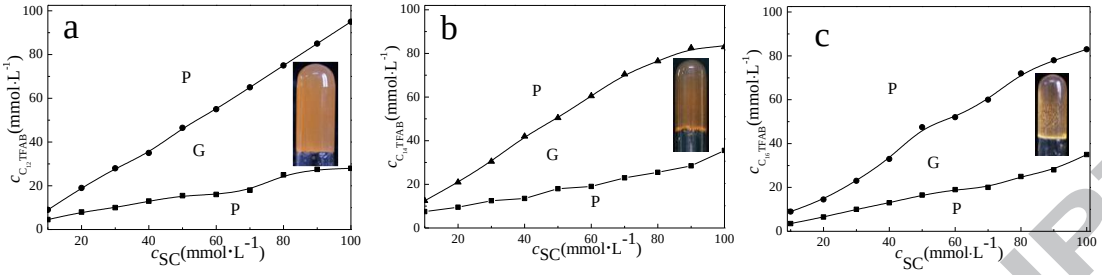

Fig. 1. Phase diagram of C_{12}TAFB/SC (a), C_{14}TAFB/SC (b), and C_{16}TAFB/SC (c) systems at 25.0 ± 0.1 ^{o}C.

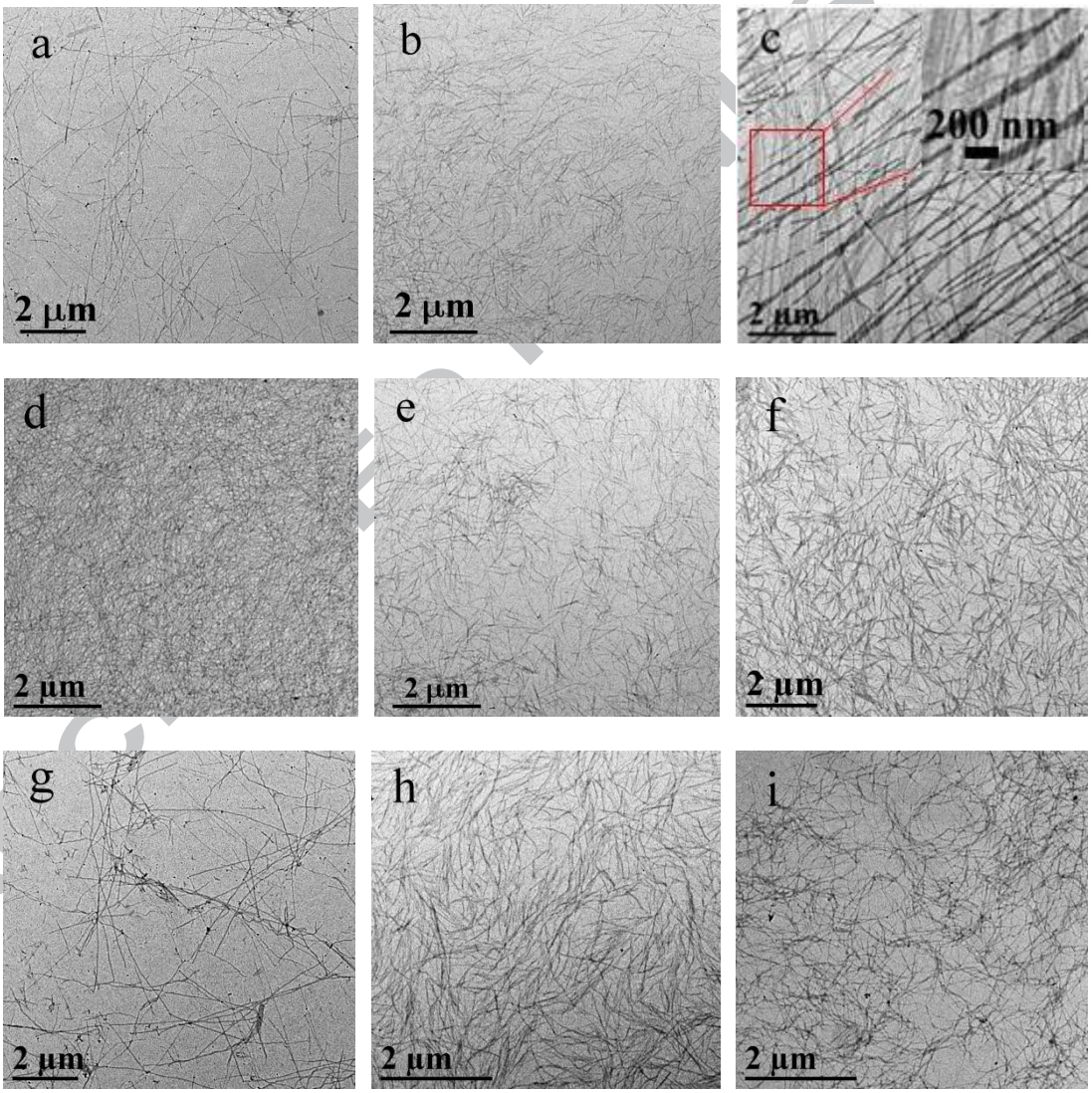

Fig. 2. TEM images of freeze-dried hydrogels formed by 20 mmol·L^{-1} SC/10 mmol·L^{-1} C_{12}TAFB (a), 40 mmol·L^{-1} SC/20 mmol·L^{-1} C_{12}TAFB (b), 50 mmol·L^{-1} SC/25 mmol·L^{-1} C_{12}TAFB (c), 60 mmol·L^{-1} SC/30 mmol·L^{-1} C_{12}TAFB (d), 50

mmol·L^{-1} SC/20 mmol·L^{-1} C_{12}TAFB (e), 50 mmol·L^{-1} SC/35 mmol·L^{-1} C_{12}TAFB (f), 50 mmol·L^{-1} SC/40 mmol·L^{-1} C_{12}TAFB (g), 50 mmol·L^{-1} SC/25 mmol·L^{-1} C_{14}TAFB (h), and 50 mmol·L^{-1} SC/25 mmol·L^{-1} C_{16}TAFB (i). An enlargement TEM image of hydrogels formed by 50 mmol·L^{-1} SC/25 mmol·L^{-1} C_{12}TAFB was inserted in (c).

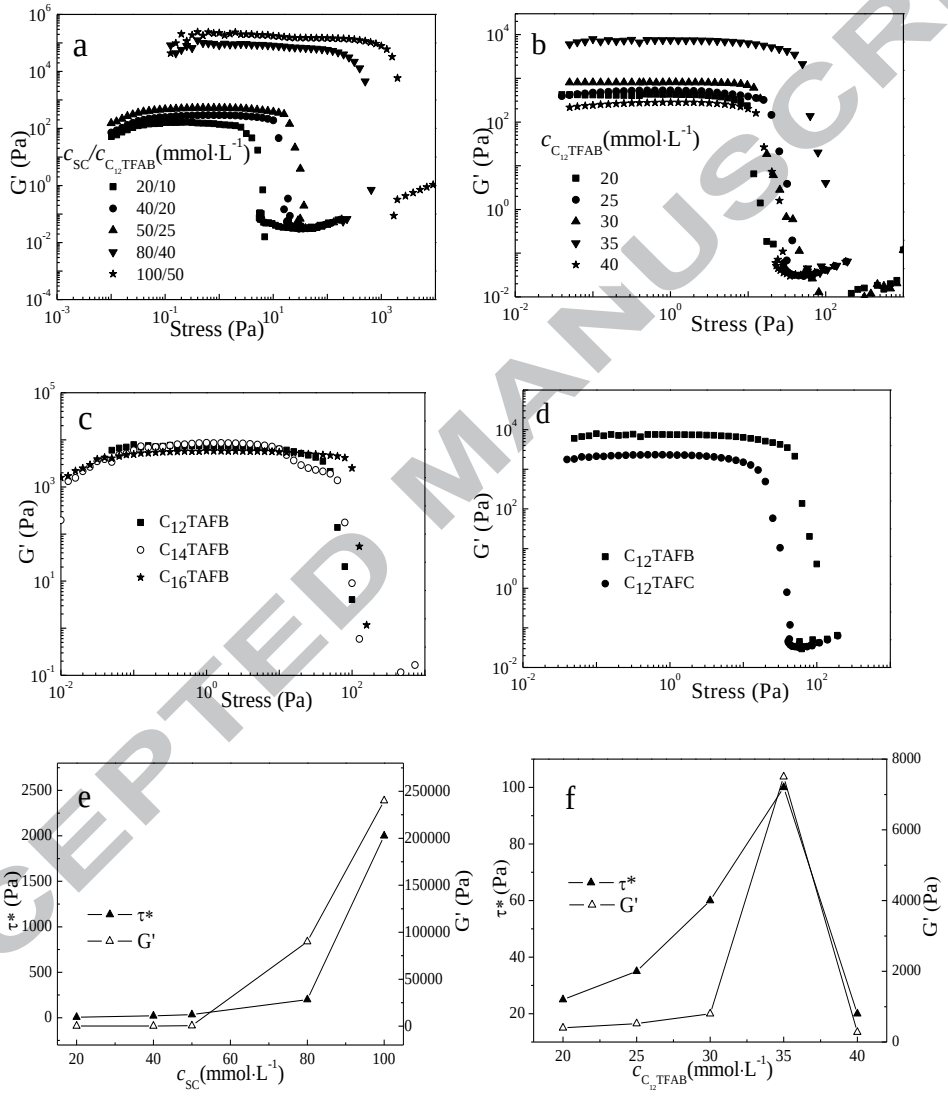

Fig. 3. G' as afunction of oscillatory stress of hydrogels formed (a) at the molar ratio of SC to C_{12}TAFB of 2:1 with different total concentrations, (b) at c_{SC} = 50 mmol·L^{-1} with different amounts of C_{12}TAFB, (c) at the different chain length (50 mmol·L^{-1} SC/25 mmol·L^{-1} C_nTAFB), and (d) at 50 mmol·L^{-1} SC/25 mmol·L^{-1} C_{12}TAFB (C). (e) G' and τ* as the function of total concentration at the molar ratio of SC to C_{12}TAFB of

2:1, (f) G' and τ* as the function of C_{12}TAFB concentration.

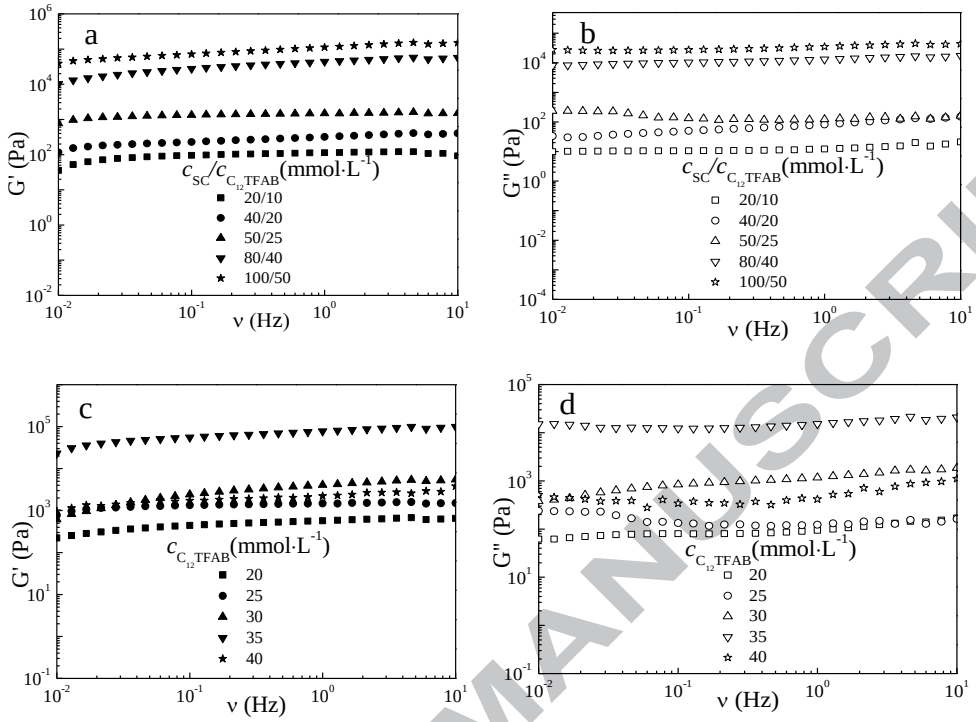

Fig. 4. G' (a) and G'' (b) as a function of frequency for the molar ratio of SC to C_{12}TAFB of 2:1 with different total concentrations; G' (c) and G'' (d) as a function of frequency for 50 mmol·L^{-1}SC with different amounts of C_{12}TAFB.

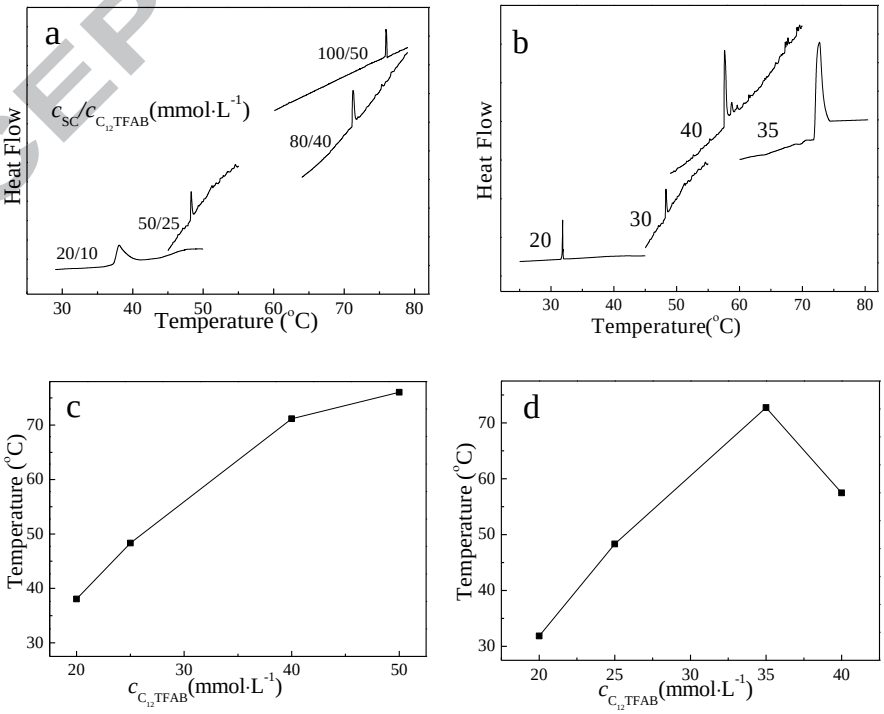

Fig. 5. (a) DSC curves of hydrogels formed by the molar ratio of SC to C_{12}TAFB of 2:1 with different total concentrations, (b) DSC curves of hydrogels formed by 50 mmol·L^{-1} SC with different amounts of C_{12}TAFB, (c) $T_{gel\text{-}sol}$ as a function of the total concentration, and (d) $T_{gel\text{-}sol}$ as a function of the concentration of C_{12}TAFB at c_{SC} = 50 mmol·L^{-1}.

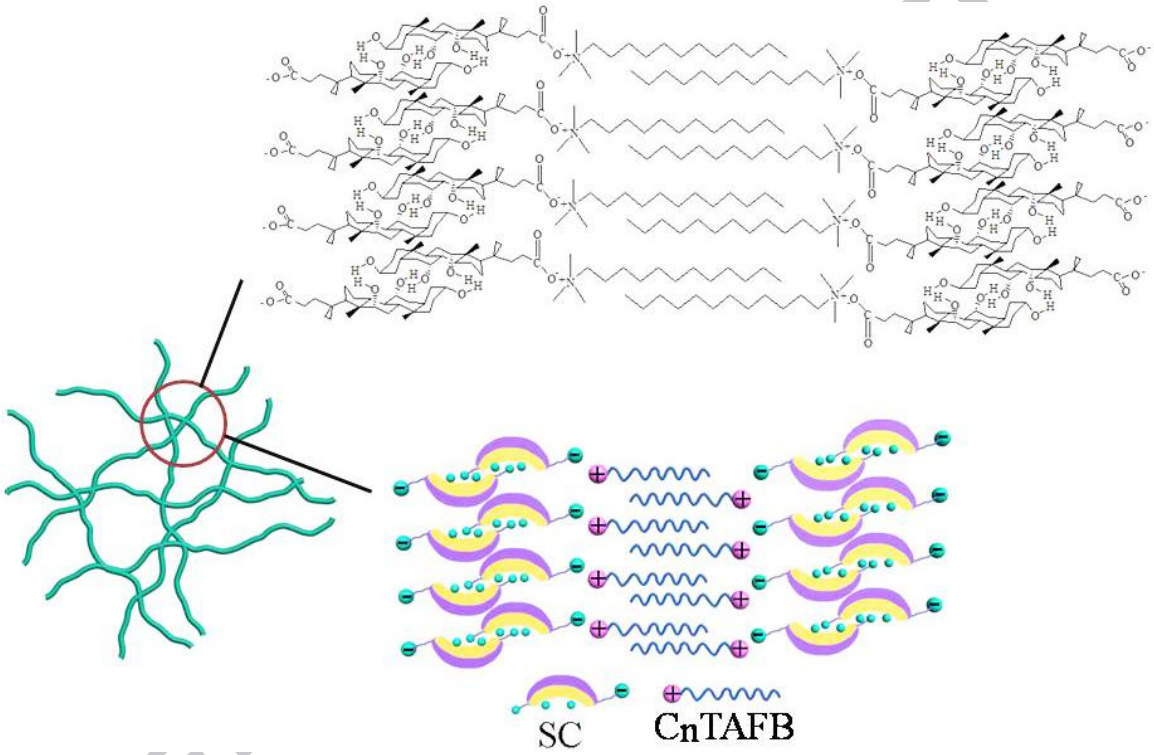

Scheme 1. Mechanism of the formation of fibers in SC/C_nTAFB hydrogels.

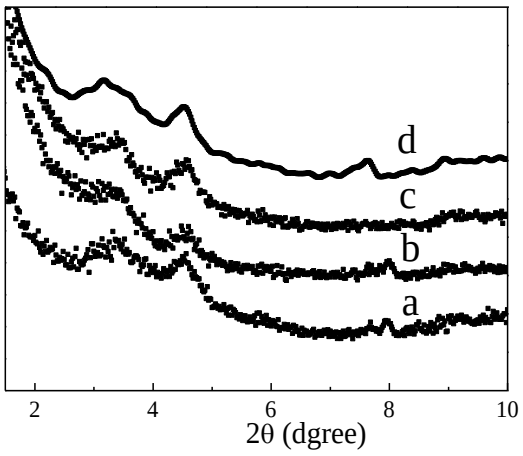

Fig. 6. SXRD patterns of dried hydrogels formed by (a) 20 mmol·L^{-1} SC/10 mmol·L^{-1} C_{12}TAFB, (b) 50 mmol·L^{-1} SC/20 mmol·L^{-1} C_{12}TAFB, (c) 50 mmol·L^{-1} SC/25

mmol·L^{-1} C_{12}TAFB, and (d) 50 mmol·L^{-1} SC/35 mmol·L^{-1} C_{12}TAFB.

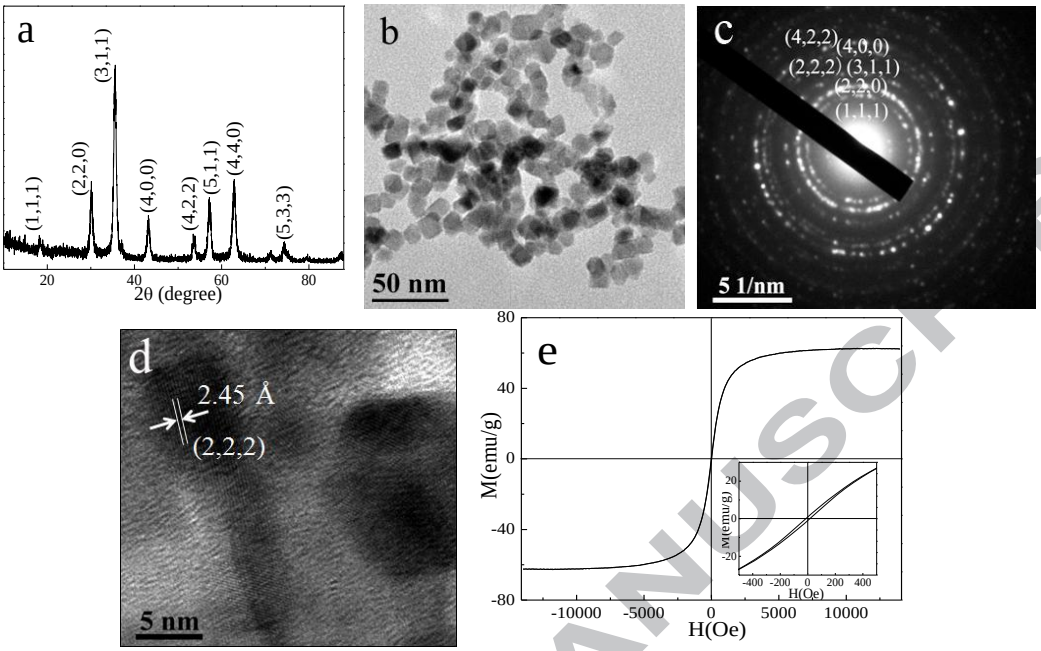

Fig. 7. a) XRD pattern, b) TEM image, c) SAED pattern, d) HR-TEM image, e)

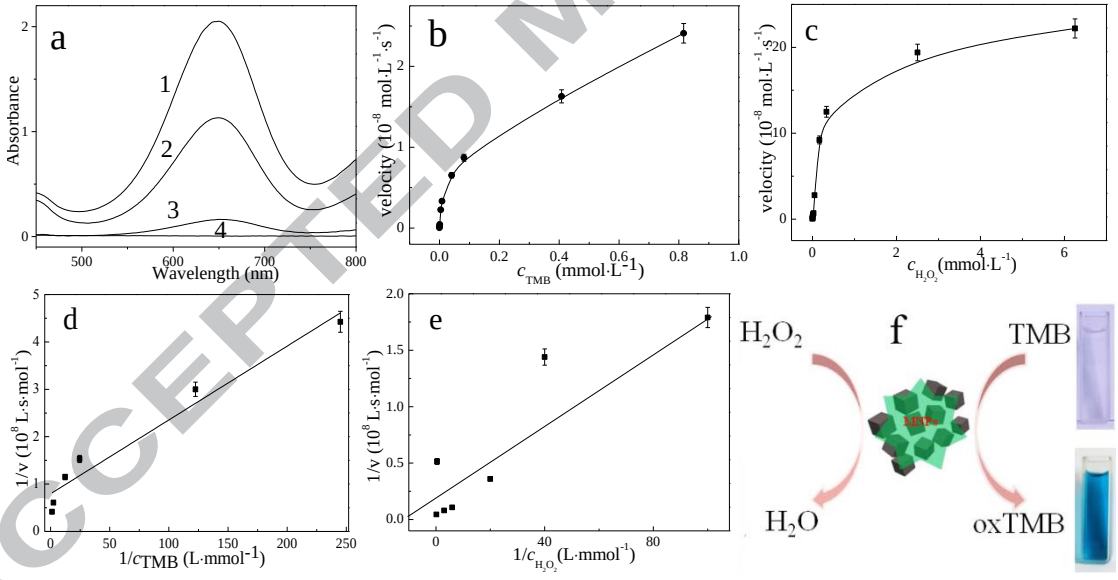

Fig. 8. (a) Typical absorption spectra of aqueous suspensions of the corresponding reactions incubated at 40 ^{o}C in acetate buffer (8 mL, 0.2 mol·L^{-1}, pH = 4.0), curve 1: 50 μg Fe_3O_4 MNPs with 816 μmol·L^{-1} TMB and 10 mmol·L^{-1} H_2O_2; curve 2: 1 ng HRP with 816 μmol·L^{-1} TMB and 10 mmol·L^{-1} H_2O_2; curve 3: 816 μmol·L^{-1} TMB and 10 mmol·L^{-1} H_2O_2 without Fe_3O_4 MNPs; and curve 4: 50 μg Fe_3O_4 MNPs and 10 mmol·L^{-1} H_2O_2 without TMB. (b-e) Steady-state kinetic assay and catalytic

mechanism of Fe_3O_4 MNPs. The velocity (v) of the reaction was measured using 50 μg Fe_3O_4 MNPs in acetate buffer (8 mL, 0.2 mol·L^{-1}, pH = 4.0) at 40 ^oC (b,c). The concentration of H_2O_2 was 10 mmol·L^{-1} and the TMB concentration was varied (b,d). The concentration of TMB was 816 μmmol·L^{-1} and the H_2O_2 concentration was varied (c,e). Schematic illustration of colorimetric determination of H_2O_2 using Fe_3O_4 MNPs catalyzed reactions (f).

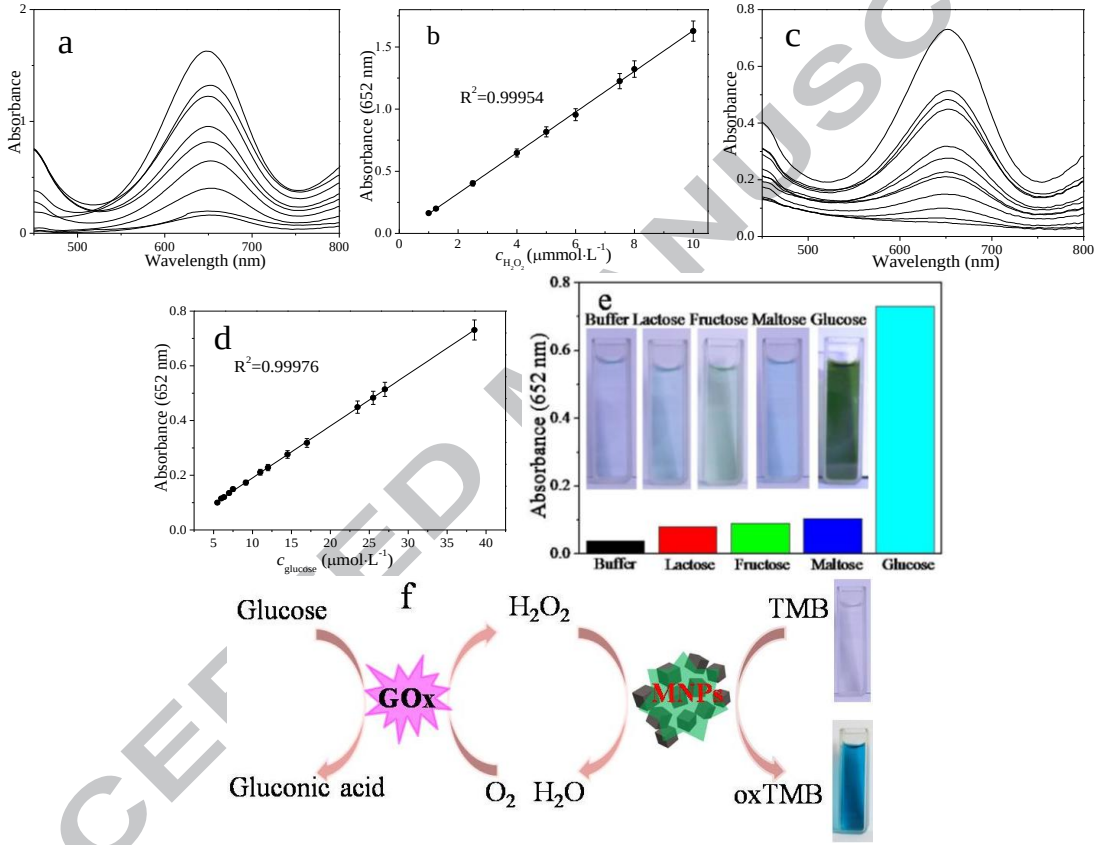

Fig. 9. H_2O_2 and glucose detection based on Fe_3O_4 MNPs. The UV-vis spectra of (a) H_2O_2 solution and (c) glucose solution with Fe_3O_4 MNPs and 816 μmol·L^{-1} TMB in acetate buffer (pH = 4.0). The concentration of H_2O_2 (μmol·L^{-1}) in (a) from top to bottom is 10, 8, 7.5, 6, 5, 4, 2.5, 1.25, and 1. The concentration of glucose (μmol·L^{-1}) in (c) from top to bottom is 38.5, 27, 25.5, 23.5, 17, 14.5, 12, 11, 7.5, 5.5, 0.00143, and 0.00016. The linear calibration plot for H_2O_2 (b) and glucose (d). Selectivity analysis for glucose detection by monitoring the absorbance at 652 nm (e), the analyte concentration were as follows: 10 mmol·L^{-1} lactose, 10 mmol·L^{-1} fructose, 10

mmol·L^{-1} maltose, and 38.5 μmol·L^{-1} glucose, inset: the color change with the different solutions. Schematic illustration of colorimetric determination of glucose using glucose (GOx) and Fe_3O_4 MNPs catalyzed reactions (f).

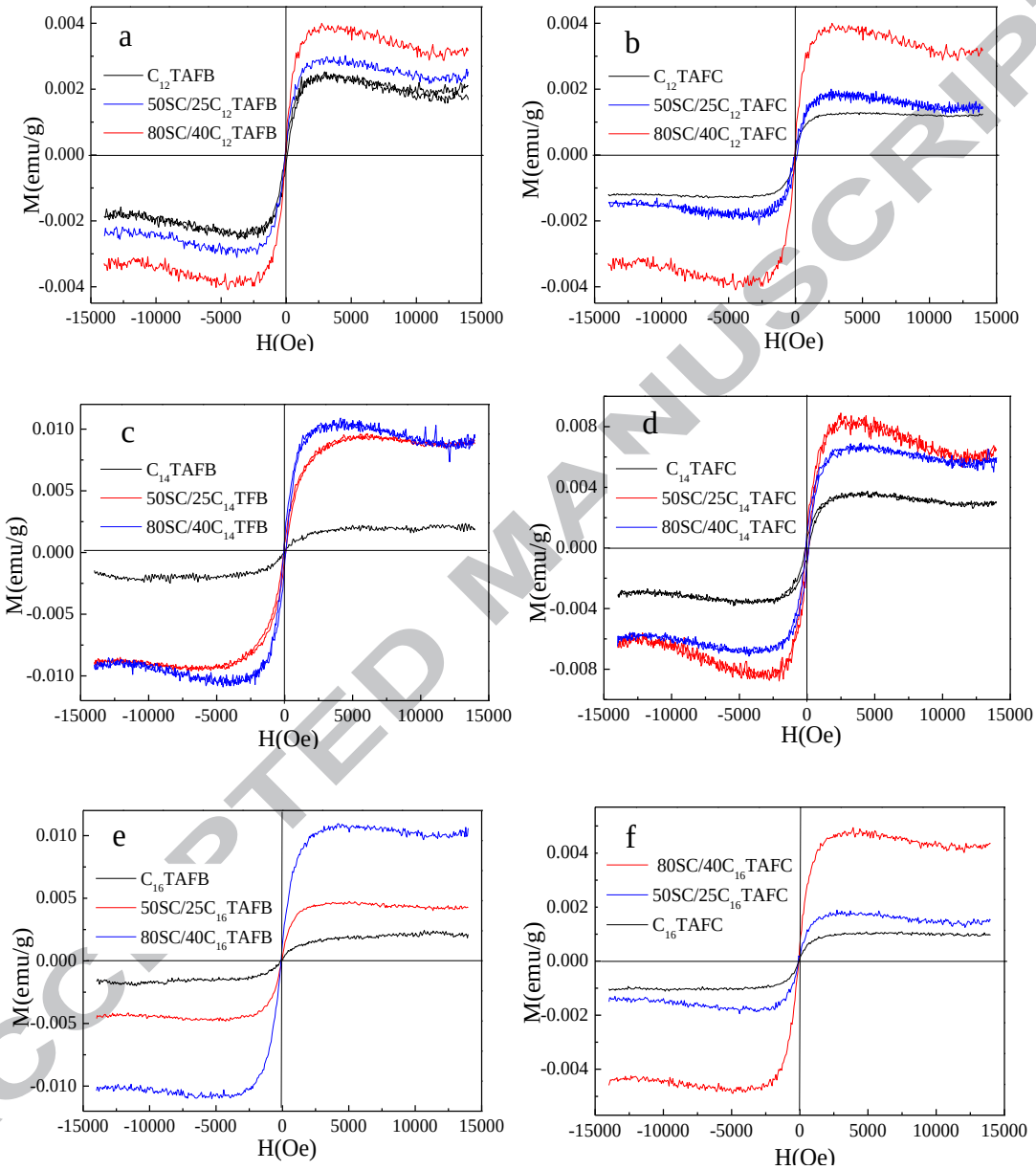

Fig. S1. Superconducting quantum interference device (SQUID) magnetometry of the magnetic surfactants, C_nTAFB (C) (n = 12, 14, 16), and the ferromagnetic C_nTAFB (C)/SC hydrogels: (a) $C_{12}TAFB$ and $C_{12}TAFB$/SC hydrogels, (b) $C_{12}TAFC$ and $C_{12}TAFC$/SC hydrogels, (c) $C_{14}TAFB$ and $C_{14}TAFB$/SC hydrogels, (d) $C_{14}TAFC$ and $C_{14}TAFC$/SC hydrogels, (e) $C_{16}TAFB$ and $C_{16}TAFB$/SC hydrogels,

and (f) C_{16}TAFC and C_{16}TAFC/SC hydrogels. the concentration (mmol·L^{-1}) of the hydrogels was inserted.

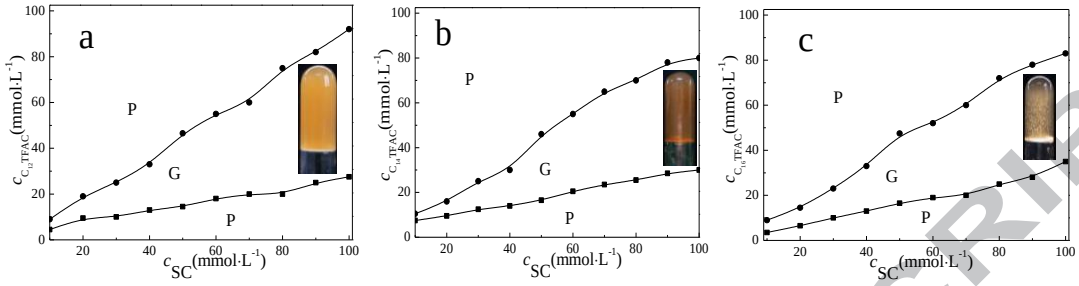

Fig. S2. Phase diagram of C_{12}TAFC/SC, C_{14}TAFC/SC, C_{16}TAFC/SC systems at T = 25.0 ± 0.1 ^{o}C.

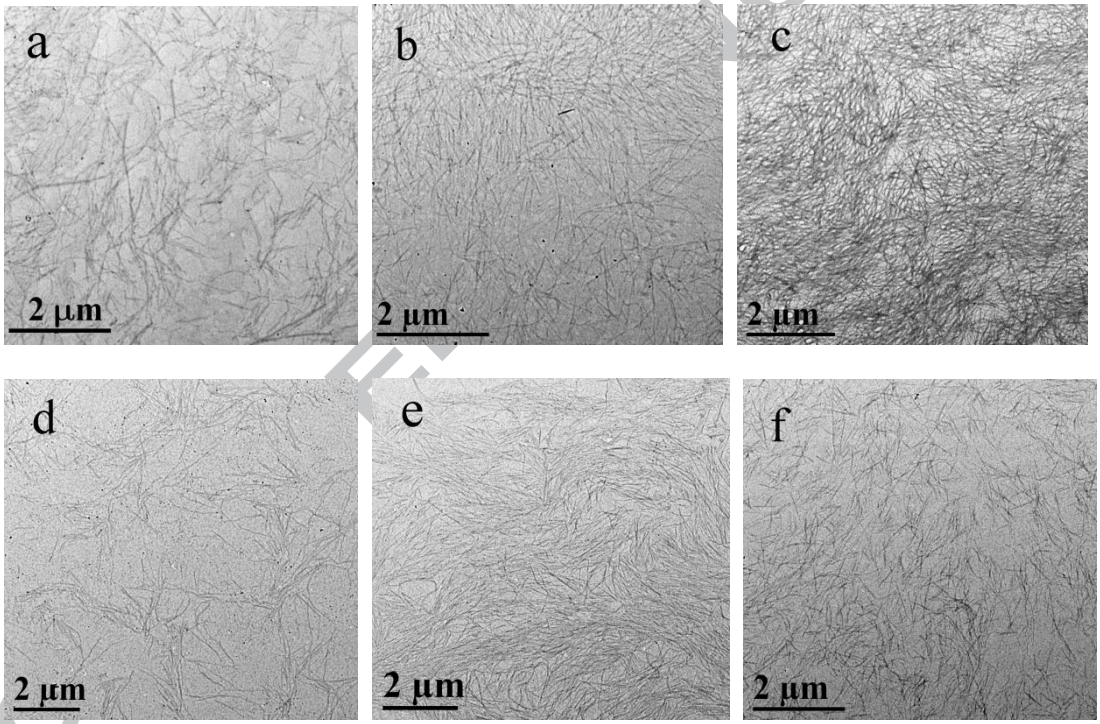

Fig. S3. TEM images of freeze-dried hydrogels formed by 20 mmol·L^{-1} SC/10 mmol·L^{-1} C_{14}TAFB (a), 40 mmol·L^{-1} SC/20 mmol·L^{-1} C_{14}TAFB (b), 60 mmol·L^{-1} SC/30 mmol·L^{-1} C_{14}TAFB (c), 50 mmol·L^{-1} SC/20 mmol·L^{-1} C_{14}TAFB (d), 50 mmol·L^{-1} SC/35 mmol·L^{-1} C_{14}TAFB (e), and 50 mmol·L^{-1} SC/40 mmol·L^{-1} C_{14}TAFB (f).

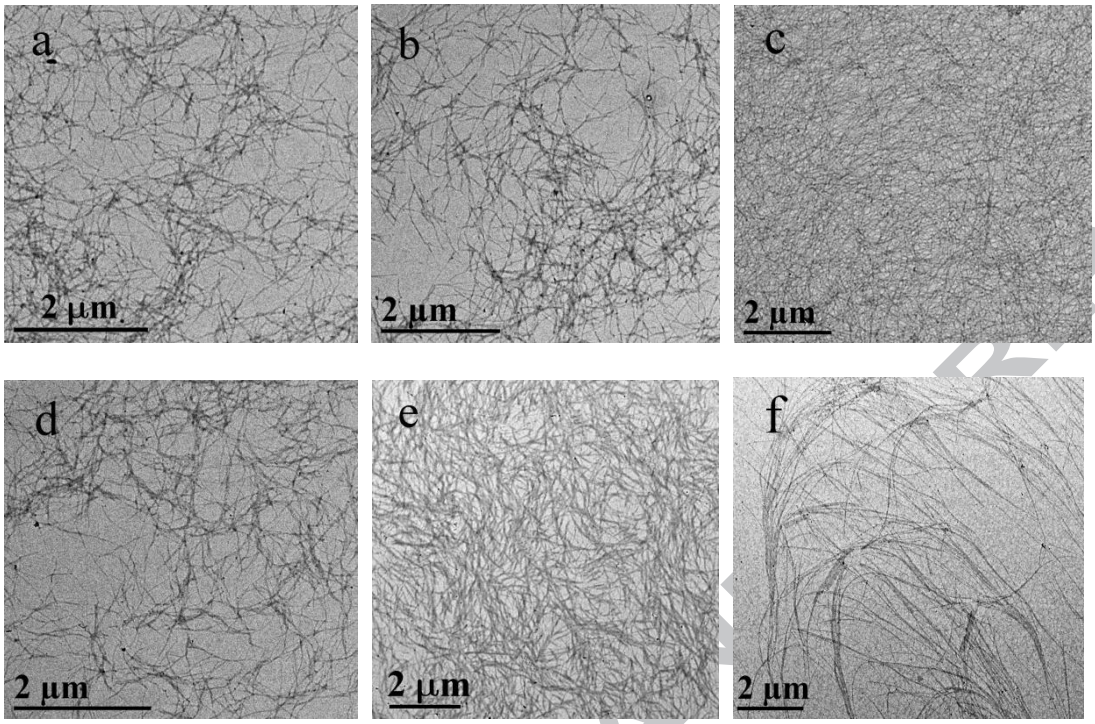

Fig. S4. TEM images of dried hydrogels formed by 20 mmol·L^{-1} SC/10 mmol·L^{-1} C_{16}TAFB (a), 40 mmol·L^{-1} SC/20 mmol·L^{-1} C_{16}TAFB (b), 60 mmol·L^{-1} SC/30 mmol·L^{-1} C_{16}TAFB (c), 50 mmol·L^{-1} SC/20 mmol·L^{-1} C_{16}TAFB (d), 50 mmol·L^{-1} SC/35 mmol·L^{-1} C_{16}TAFB (e), and 50 mmol·L^{-1} SC/40 mmol·L^{-1} C_{16}TAFB (f).

Fig. S5. Reversible stimuli-responsive transition of hydrogels (50 mmol·L^{-1} SC/25 mmol·L^{-1} C_{12}TAFB) triggered by shearing force and temperature.

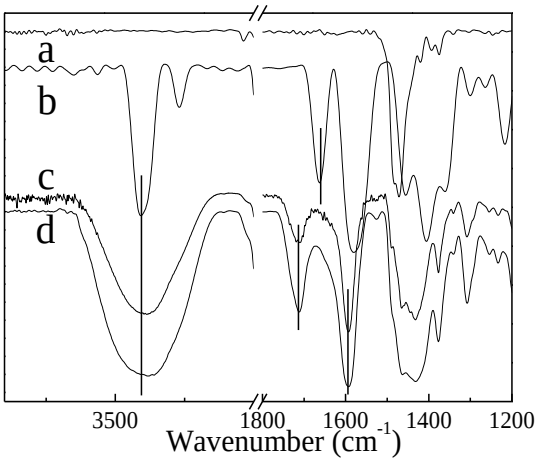

Fig. S6. FT-IR spectra of C_{12}TAFB (a), SC (b), xerogels formed by 50 mmol·L^{-1} SC/25 mmol·L^{-1} C_{12}TAFB (c) and 100 mmol·L^{-1} SC/50 mmol·L^{-1} C_{12}TAFB (d).

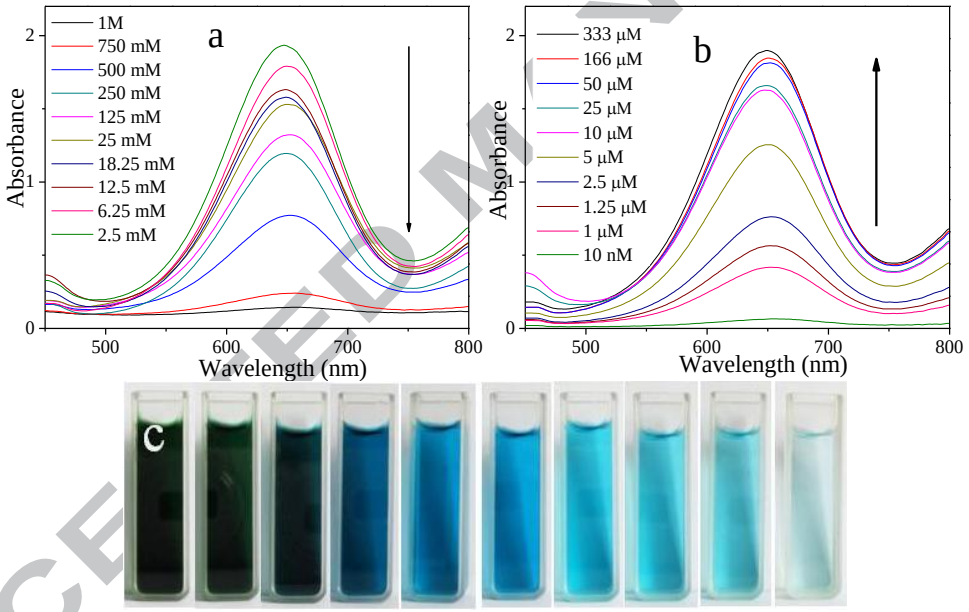

Fig. S7. H_2O_2 detection based on peroxidase-like Fe_3O_4 MNPs. The UV-vis spectra of H_2O_2 solution with Fe_3O_4 MNPs and 816 μmol·L^{-1} TMB in acetate buffer (a, b). The images of color reaction of TMB with different concentrations of H_2O_2, the concentration of H_2O_2 (μmol·L^{-1}) from left to right is 1000, 500, 100, 50, 10, 5, 2.5, 1.25, 1, 0.01 (c).

Table 1 Gelation behavior of C_nTAFB (C) and sodium salts of bile acid systems in aqueous solutions at 25 ^oC

	Chain length (nm)[50]	**Aggregates**			***CGC*[a] (wt %)**			**Gelation time**			**Gelation number[b]**		
		SC	SDC	SLC	SC	SDC	SLC	SC	SDC	SLC	SC	SDC	SLC
$C_{12}TAFB$	1.672	G[c]	G	P[d]	0.329	0.282		48 h	96 h		7936	9259	
$C_{12}TAFC$	1.672	G	G	P	0.320	0.270		72 h	108 h		7407	8547	
$C_{14}TAFB$	1.925	G	G	P	0.249	0.224		36 h	48 h		11111	12345	
$C_{14}TAFC$	1.925	G	G	P	0.250	0.227		40 h	54 h		10101	11111	
$C_{16}TAFB$	2.178	G	G	P	0.211	0.184		30 h	36 h		13888	14873	
$C_{16}TAFC$	2.178	G	G	P	0.217	0.193		36 h	48 h		12345	13888	

[a]*CGC*: critical gelation concentration; [b]Gelation number: the maximum number of solvent molecules immobilized by gelator molecules;[44] [c]G: Gels; [d]P: precipitates.

SQUID magnetometry of Fe_3O_4 MNPs prepared from SC/$C_{12}TAFB$ hydrogel.

Table 2 Michaelis constant (K_m) and maximal reaction rate (V_{max}) of Fe_3O_4 MNPs.

catalyst	substrate	K_m(mmol·L^{-1})	V_{max} (10^{-8} mol·L^{-1}·s^{-1})
Fe_3O_4 MNPs	TMB	0.091	5.18
	H_2O_2	0.01957	1.26
HRP	TMB[27]	0.434	10.0
	H_2O_2[27]	3.70	8.71

Table S1 Dynamic rheology of SC/C_{12}TAFB hydrogels. The G' and G" values were obtained from frequency sweep experiments

SC /C_{12}TAFB (mmol·L^{-1})	Storage modulus, G' (Pa)	Loss modulus, G" (Pa)	Stiffness, (G'/G")
20/10	120	12	10
40/20	360	60	6
50/25	1500	120	12.5
80/40	45000	10000	4.5
100/50	130000	30000	4.3

Table S2 Dynamic rheology of 50 mmol·L^{-1} SC/C_{12}TAFB hydrogels. The G' and G" values were obtained from frequency sweep experiments

50 mmol·L^{-1} SC/C_{12}TAFB (mmol·L^{-1})	Storage modulus, G' (Pa)	Loss modulus, G" (Pa)	Stiffness, (G'/G")
20	600	80	7.5
25	1500	150	10
30	4500	900	5
35	80000	15000	5.3
40	2000	400	5

Graphical abstract:

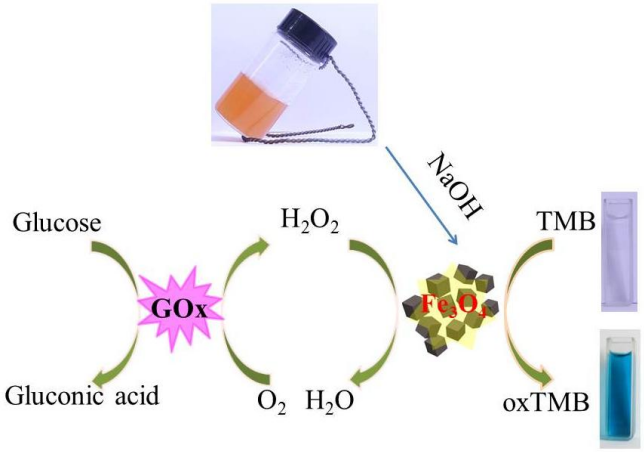

Fe_3O_4 nanoparticle prepared based on C_{12}TAFB/SC hydrogels acted as a biosensor for H_2O_2 and glucose detection.